Interrogation of inter-layer neuronal connectivity via cross-region all-optical physiology with high temporal resolution

Authors: Chi Liu[1, †], Yuejun Hao[3,4,5, †], Yi Zhong[3,4,5]*, Lingjie Kong[1,4]*, Bo Lei[2,4,5]*

Affiliations:

[1] State Key Laboratory of Precision Measurement Technology and Instruments, Department of Precision Instrument, Tsinghua University, Beijing 100084, P.R. China.

[2] Beijing Academy of Artificial Intelligence, Beijing 100084, P.R. China.

[3] School of Life Sciences, Tsinghua University, Beijing 100084, P.R. China.

[4] IDG/McGovern Institute of Brain Research, Tsinghua University, Beijing 100084, P.R. China.

[5] Tsinghua-Peking Center for Life Sciences, Tsinghua University, Beijing 100084, P.R. China.

[†] These authors contributed equally.

*Correspondence: **Bo Lei**: b.lei.2022@hotmail.com; **Lingjie Kong**: konglj@tsinghua.edu.cn; **Yi Zhong**: zhongyithu@tsinghua.edu.cn

Abstract:

The interrogation of functional neural circuits is crucial for uncovering how the brain works during diverse behaviours. Multi-area neurophysiological measurement systems with high temporal resolution are indispensable, especially for dissecting inter-region functional connectivity. Here, we develop a cross-region all-optical physiology system (CRAOP) that enables the simultaneous recording and manipulation of single-neuron activities in multiple brain areas. Based on spatiotemporal multiplexing, our system enables all-optical analysis in the cortex and hippocampus with a high frame rate and minimal time delay in inter-layer imaging and photostimulation. Combined with behavioural experiments, CRAOP provides all-optical evidence linking behavioural responses to neuronal connectivity in the primary visual cortex (V1) in live mice. Furthermore, we demonstrate that CRAOP can perturb the activity response of interregional cortical neurons to sensory stimuli according to their functional signatures. Overall, CRAOP provides an optical approach for mapping interlayer connectivity at the single-neuron level and for modifying neuronal responses in behaving animals.

Introduction

Revealing the connectome of the brain is crucial for understanding its functions and dysfunctions(*1*, *2*). Diverse approaches have been developed to dissect the anatomical or functional connectivity of individual neurons, such as single-neuron electrophysiology(*3–7*) and electron microscopy-mediated tissue reconstruction(*8–14*). Although these approaches provide the most precise measurements for physiological or physical local connectivity, respectively, they still face challenges in high-throughput analysis with behavioral stimuli. Recently, a proposed solution to address this limitation is all-optical physiology (AOP), which integrates simultaneous activity readout and manipulations within live animals(*15–26*). Combining calcium/voltage imaging with optogenetics, the AOP system can noninvasively, rapidly, and precisely acquire the local connectivity and identify the functional signature of specific neurons(*18*, *20*, *25*, *27–29*). Moreover, AOP offers another significant advantage through its high compatibility with behavioral stimuli. When combined with behavioral approaches, the AOP strategy has the potential to generate artificially induced ensembles(*18*, *26*), control sensory-guided behavior(*17*, *20*), and implement closed-loop control over neuronal activity patterns in awake mice(*24*, *27*). However, these approaches are limited by the available field-of-views (FoVs) of imaging systems, making it difficult to dissect interregional functional connectivity with high temporal resolutions. Therefore, extending the two-photon AOP to the cross-region level with high temporal fidelity is essential for dissecting interregional functional connectivity.

In this study, we present the Cross-Region All-Optical Physiology (CRAOP) system, which integrates spatiotemporal multiplexing-based two-photon imaging with single-neuron optogenetics. This innovative system enables the simultaneous recording and manipulation of neural networks across brain regions with axial intervals as large as 530 μm, and the temporal resolution in two-plane imaging can be on the scale of sub milliseconds (up to 12.5 ns temporal sampling with 1x1 pixel spatial sampling). We demonstrate the superior performance of CRAOP in interrogating inter-layer neuronal connectivity by in vivo imaging and manipulation of neural circuits in the cortex and hippocampus of mouse brains. First, we demonstrate the simultaneous recording of neurons at different layers to identify behavior-specific neurons. Subsequently, we selectively excite these function-specific neurons while maintaining synchronous recording of neurons at multiple layers, enabling analysis of inter-layer connectivity. Importantly, this synchronized optical manipulation and recording of neuronal activities across long-distance layers in cortical columns in vivo allow us to manipulate selected neurons to achieve inter-layer modification of neural responses to behavior. We expect that CRAOP will facilitate a broad array of novel

approaches in neural connectome studies while also inspiring new applications for interacting with the brain.

Results

CRAOP system for simultaneous recording and manipulation of interregional neural networks

In the CRAOP system, simultaneous imaging across different planes with high temporal resolution is a major challenge. While several components, such as piezoelectric displacement stages, electrically tunable lenses (ETLs)(*30*), deformable mirrors(*31*), voice coils(*32*), and ultrasonic phase-locked lenses(*33*), have been developed for fast axial scanning, simultaneous recording of two brain regions with significant axial separation remains difficult. To overcome this obstacle, we adopted spatiotemporal multiplexing(*34–39*) in our custom-built two-photon microscopes (Fig. 1A and B). We focused one excitation beam at the aplanatic plane of the objective lens (Path 1) for optimal deep imaging quality while biasing the other beam upwards by up to 500 μm (Path 2) to cover a large axial range. The time delay between these two imaging beams is approximately 6.25 ns, thus ensuring the acquisition of neuronal activity with high temporal fidelity. The stimulation beam is parfocal with the imaging beam, which focuses on the deeper plane. The spiral scan strategy is adopted to photostimulate neurons expressing optogenetic tools.

To record neural activities at multiple cortical layers, we further inserted an electrically tunable lens (EL-16-40-TC, Optotune) into Path 2 to rapidly switch imaging planes. Moreover, by combining offset lenses of 75 mm focal length with objective lenses (CFI75 LWD 16X W, Nikon), axial imaging ranges as large as 530 μm can be achieved. We quantified the two-photon spatial resolution using 0.5 μm fluorescence beads. The lateral full-width-at-half-maximums (FWHMs) are 0.7 ± 0.1 μm (mean ± s.d.) and 1.1 ± 0.1 μm at the lower plane (Path1) and the upper plane (Path2), respectively, while the axial FWHMs are 10.6 ± 0.1 μm and 22.0 ± 0.5 μm at the lower plane (Path1) and the upper plane (Path2), respectively (Fig. 1, D and E). The numerical aperture (NA) of the stimulation path is higher than those of the imaging paths to improve the spatial localization and photostimulation efficiency of two-photon optogenetics, and the lateral and axial FWHMs of the stimulation path are 0.6 ± 0.1 μm and 7.3 ± 0.4 μm, respectively (Fig. 1C). This system not only provides the ability to investigate laterally connected neurons within the same objective FoV but also infers and analyzes neurons with functional correlations located at different depths.

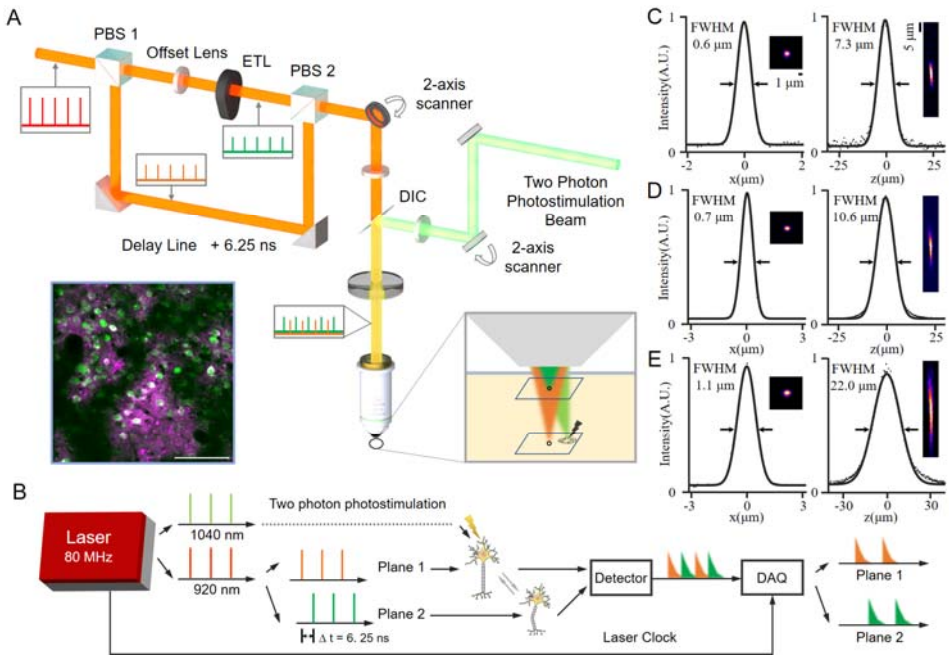

Fig. 1 System schematics of the cross-region all-optical physiology system. (**A**) System diagram of the simultaneous multiphoton recording and manipulating system. Inset (lower left): Representative image of neurons expressing both GCaMP6s (green) and C1V1-mCherry (magenta), PBS: polarization beam splitter, DIC: Dichroic mirror. Scale bar: 80 μm. Inset (lower right): Diagram of the postobjective optical paths. Optogenetic foci are located at the lower plane. The axial distance between the upper plane and lower plane is adjusted by an electronic tunable lens. (**B**) Signal flow diagram of the cross-region all-optical physiology system. (**C**) Cross-sectional plots of the focal profile of the photostimulation beam. FWHM full width at half maximum. (**D**) Cross-sectional plots of the focal profile of the lower plane imaging beam. (**E**) Cross-sectional plots of the focal profile of the upper plane imaging beam.

High-speed cross-plane imaging of neuronal activity in vivo via CRAOP

We next demonstrated the capability and advantages of our CRAOP system for simultaneously imaging two axially separated layers of neurons at high temporal resolution in several scenarios. First, we performed in vivo dual-plane imaging of the mouse V1 cortex expressing GCaMP6s at two different depths (100 μm and 530 μm) with a 540 × 540 μm2 FOV at 60 Hz in anaesthetized mice (Fig. 2, A and B). This enabled the detection of a substantial population of active neurons from both planes, facilitating further analysis of population activity patterns and coactivities among neurons within and across planes. Neurons exhibiting high cross-correlations of calcium activities were identified, suggesting potential functional connectivity (Fig. 2,

C to E). Next, we further demonstrated the dual-plane recording of neuronal activities from the deep and superficial layers of hippocampal CA1 expressing GCaMP8m (*40*). Despite these two layers being separated by only 50 μm, we could separate the activity traces of neurons from both layers with high quality (Fig. 2, F to H) and identify possible functional connections between neurons in CA1 via activity correlation (Fig. 2, I and J).

Importantly, our CRAOP system has a delay of fewer than 10 ns between two imaging planes, far less than other methods such as ETL-based methods (*19*, *23*, *26*, *41*). Thus, the CRAOP system allows dual-plane imaging with high temporal precision, which is suitable for high-frame-rate imaging of neuronal signals. We used the CRAOP system to perform high-speed dual-plane cortex calcium imaging (396.1 Hz) and identify the sequence of firing among highly correlated neurons from two neuronal layers (Fig. 2, K to N). Using our system, we could identify the short delay times between the onset of calcium events in neurons from different planes (Fig. 2, M and N). We also performed high-speed recording (60 Hz) of local GABA signals(*42*) from two neuronal layers, further demonstrating the diverse imaging modalities recordable by our system (fig. S6).

By combining a switchable offset lens before the ETL, the axial interval between two imaging planes and the total number of sampled planes can be further adjusted. We performed multi-plane imaging in mouse cortex S1 spanning over a 500 μm distance, resulting in near-volumetric imaging and analysis of coactivities in a large number of neurons in a 3D volume (Fig. 2, O to S). Our design led to a frame rate of 30 Hz in the lower plane and a volume rate of 10 Hz in the upper range. To avoid the override effect of the ETL, the duty cycle of the image was reduced to 50%. Finally, only 256 × 256 pixels were retained (Table S1). These results demonstrated the versatility of the CRAOP system for studying a variety of brain regions and for different scenarios where high-speed or multi-plane sampling is required.

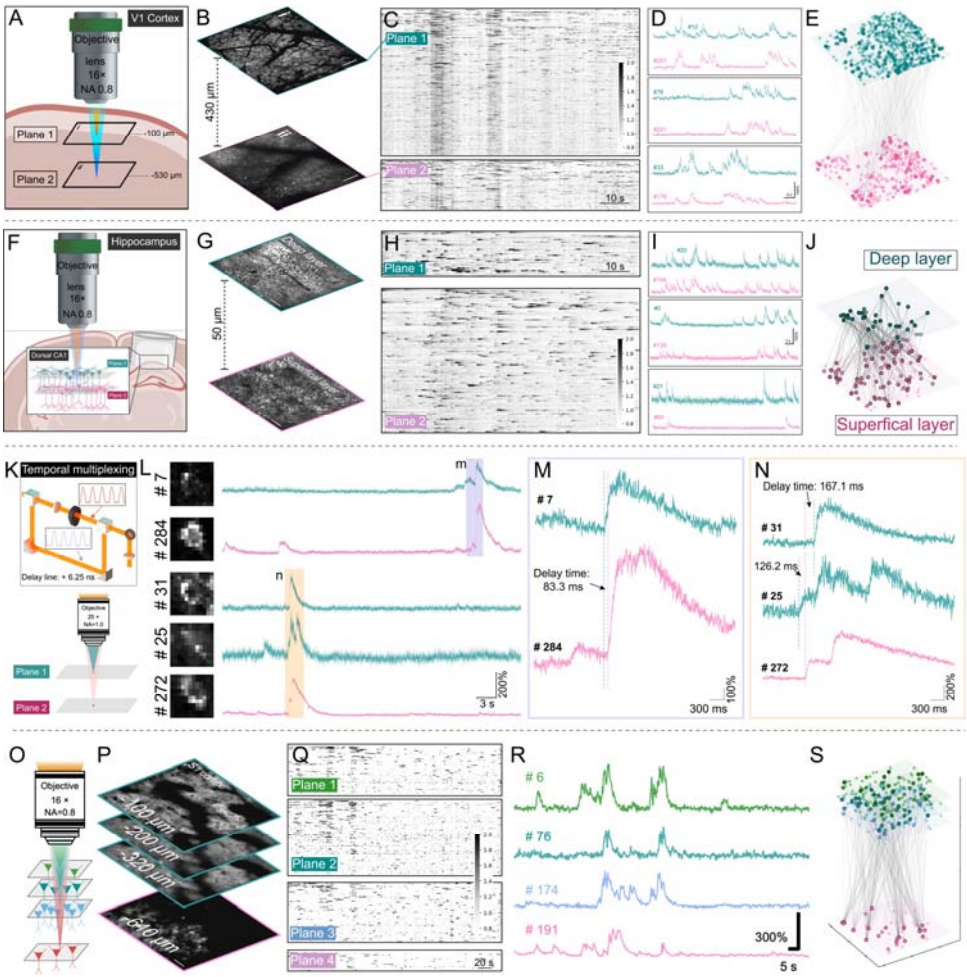

Fig. 2 Simultaneous dual-plane recording of mouse neuronal activity. (**A**) Diagram of dual-plane imaging in the mouse V1 cortex. (**B**) Representative images of two planes simultaneously acquired in the mouse V1 area. Scale bar: 90 μm. (**C**) Neural activities of recorded neurons in both regions. (**D**) Activities of selected neurons from the dual plane. (**E**) 3D demonstration of all recorded neurons from dual-plane recording. Lines connecting neurons indicate a high correlation in activity (Corr>0.55) (**F**) Diagram of dual-plane imaging in mouse hippocampal CA1. (**G**) Representative images of two planes simultaneously acquired in mouse hippocampal CA1. Scale bar: 35 μm. (**H**) Neural activities of recorded neurons in both regions. (**I**) Activities of selected neurons from the dual plane. (**J**) 3D demonstration of all recorded neurons from dual-plane recording. Lines connecting neurons indicate a high correlation in activity (Corr>0.30) (**K**) Diagram of high frame rate (>396 Hz) dual plane imaging in mouse cortex (Axial interval: 50 μm). (**L**) Activities of selected neurons with similar activity traces from the dual plane. (**M**) Zoomed-in trace of neurons highlighted purple in (L). (**N**) Zoomed-in trace of neurons highlighted yellow in (L). (**O**) Diagram of four-plane imaging in the mouse S1 cortex. (**P**) Representative images of the four planes acquired in the

mouse S1 cortex. Scale bar: 40 μm. (**Q**) Neural activities of recorded neurons in four layers. (**R**) Activities of selected neurons from four layers. (**S**) 3D demonstration of all recorded neurons from four-plane recording. Lines connecting neurons indicate a high correlation in activity (Corr>0.55).

Identification of single-neuron functional connectivity between different brain regions via CRAOP

The combination of two-photon imaging and optogenetics is a powerful strategy for dissecting functional connectivity patterns among neurons(*16*, *17*, *22–24*). However, most systems do not allow connectivity analysis across axially spaced layers of neurons, which is a key question in neural circuit studies (*43*, *44*). The design of the CRAOP system allows simultaneous dual-plane imaging and single-cell optogenetics, thus it has the potential to perform across-layer functional connectivity dissection. To test this potential, we first performed CRAOP on the mouse CA3 region. Two layers of neurons were recorded at 60 Hz, while optogenetic stimulation of selected neurons expressing ChRmine(*17*) was performed in the lower plane (Fig. 3A and B). Optogenetic activation of neurons in the deeper position can elicit activity of other non-targeted neurons, consistent with studies showing the existence of recurrent connections between CA3 neurons(*45*, *46*) (Fig. 3, C and D). We also used the CRAOP system to probe interlayer functional connectivity in the mouse S1 cortex (fig. S7) and CA1 (fig. S8). Notably, correlation structures generated only from recorded spontaneous activity between neurons generally could not persist across different time points. However, optogenetic stimulation-mediated coactivation patterns remained stable (fig. S9), which demonstrated that CRAOP-mediated analysis of functional connectivity is more reliable than analysis based on calcium recording only.

Utilizing the ability of our system to achieve cross-plane measurement with high temporal resolution (high imaging frame rate and minimal time delay), we tested the potential of CRAOP to detect the voltage indicator JEDI-2P(*47*) and perform optogenetics with C1V1(*48*) in CA1 (Fig. 3E). Spiking events of neurons from two layers can be precisely visualized and aligned for detailed analysis of cofiring (Fig. 3, F to H). Photostimulation-induced depolarizing events on the targeted neurons and spiking events on other neurons could also be detected (Fig. 3, I and J), showing the significant advantage of CRAOP for interrogating neural connectivity via sensitive indicators. To dissect neuronal connectivity from multiple layers, we next employed ETL in our system to allow 3D imaging and simultaneous recording and manipulation on a separate plane (Fig. 3K). The imaging setup led to a frame rate of 30 Hz in the deeper plane and a volume rate of 10 Hz in the upper range. We applied this strategy in the mouse S1 cortex expressing GCaMP6f and C1V1 (Fig. 3, L to N).

Non-activated neurons that responded to the photostimulation event were identified, implying possible functional connectivity between the targeted neurons (Fig. 3, O and P). This strategy effectively extends the pool of recorded neurons and is suitable for inter-layer connectivity dissection using fast and sensitive activity indicators such as GCaMP8(*40*) and voltage sensors(*47*, *49*, *50*).

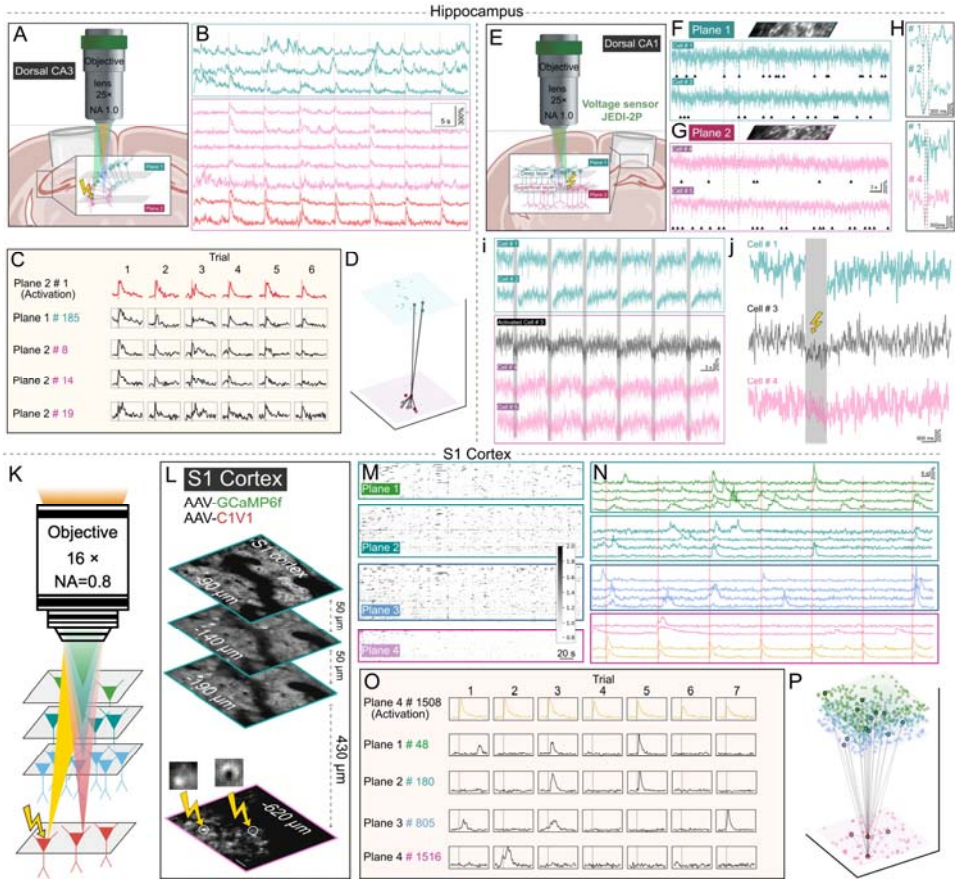

Fig. 3 Dual-plane and 3D recording combining optogenetic manipulation. (**A**) Diagram of dual-plane recording with optogenetic manipulation in mouse hippocampal CA3 (Axial interval: 50 μm). (**B**) Activities of selected neurons from the dual plane. (cyan: upper plane, pink: lower plane, red: target cell) (**C**) Responses of the target neuron and other neurons to two-photon photostimulation. (**D**) 3D demonstration of all recorded neurons from dual-plane recording with optogenetic manipulation. Lines connecting neurons indicate a high correlation between other neurons shown in (B) and the target neuron. (**E**) Diagram of dual-plane recording with optogenetic manipulation in mouse hippocampal CA1 expressing the voltage indicator (Axial interval: 50 μm). (**F**) Representative voltage signal traces of neurons in the deep layer. Fov: 160 30 μm. Arrows indicate putative spikes. (**G**) Representative voltage signal traces of neurons in the superficial layer. Fov: 160 30 μm. Arrows indicate putative spikes. (**H**) Zoomed-in trace of neurons in (F) and (G). (**I**)

Voltage traces of neurons in two layers with optogenetic activation. (J) Zoomed-in traces of neurons in (I). (**K**) Diagram of four-plane recording with optogenetic manipulation in the mouse S1 cortex. (**L**) Representative images of four planes acquired in the mouse S1 cortex with optogenetic manipulation of two target cells indicated with white circles. Scale bar: 40 μm. (**M**) Neural activities of recorded neurons in four planes. (**N**) Activities of selected neurons from four planes. (**O**) Responses of the target neurons and other neurons to two-photon photostimulation. (**P**) 3D demonstration of all recorded neurons from four-plane recording. Lines connecting neurons indicate a high correlation between other neurons shown in (N) and the target neurons.

Analysis of functional connectivity between behavior-responsive neurons in V1

In light of the promising potential of CRAOP for mapping inter-layer functional connectivity, we next combined connectivity mapping with behavioral analysis. Previous studies have utilized neuronal activity imaging and various connectivity mapping techniques, such as electrophysiology(*3*, *51*), electron microscopy(*12*, *13*), and rabies tracing(*52*, *53*), to investigate whether neurons with similar functional responses are more likely to connect in the visual cortex. In this study, we employed the CRAOP system to address this question specifically in mouse V1 layer 2/3.

Here, we investigated the functional connectivity of mouse V1 layer 2/3 neurons using the CRAOP system. Specifically, we expressed GCaMP8m and rsChRmine(*54*) tto enable simultaneous recording and manipulation of neuronal activity in vivo via a cranial window. Drift grating visual stimuli were first presented to the mouse while the system recorded the activity of two neuronal layers separated by 50 μm (Fig. 4, A to D). Next, we photostimulated selected neurons and recorded the responses of all neurons from both layers to this optogenetic stimulus (Fig. 4, E to G). We observed a positive correlation between the coupling strength of neuronal pairs measured by CRAOP and their activity correlation during visual stimulation (Fig. 4, H and I). This finding is consistent with previous studies demonstrating that functional activity correlation or similar stimulus selectivity positively correlates with the likelihood of neuronal connectivity at various levels (*52*, *53*). A similar result was also obtained by CRAOP when mice were given movies as visual stimuli (fig. S10). Importantly, our method allows a broader sampling of cortical layers in both axial and lateral directions and is repeatable in the same animal.

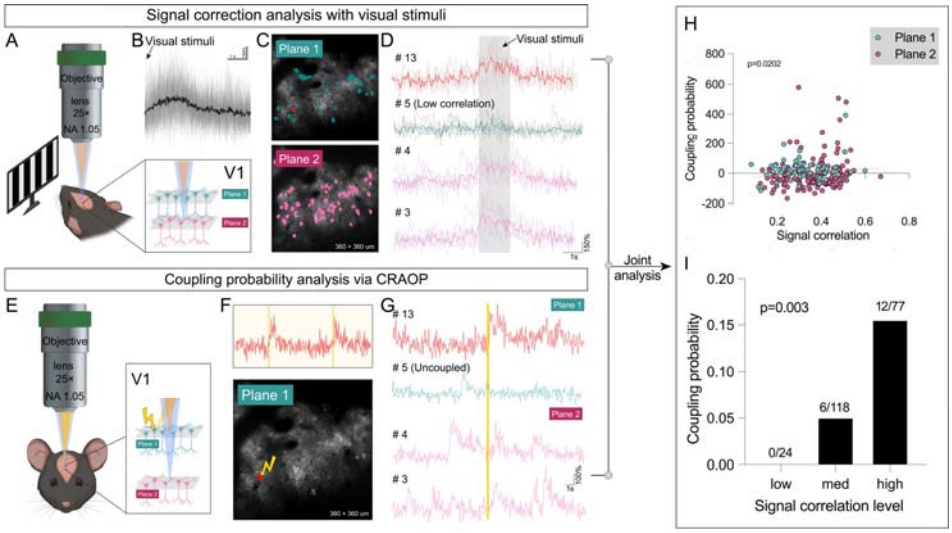

Fig. 4 CRAOP analysis of functional connectivity with stimulus response correlation in V1. (**A**) Diagram of dual-plane recording in V1 with visual stimuli. (**B**) Averaged activity trace of recorded neurons in response to the visual stimuli. (**C**) Example of spatial masks of recorded neurons in one trial (cyan: upper plane cells, pink: lower plane cells, red: cell to be photostimulated). (**D**) Example of activity traces of selected neurons (#13 is the cell to be stimulated; #5 has a low signal correlation with it; #3 and #4 have a high signal correlation with it). (**E**) Diagram of dual-plane recording and targeted photostimulation in V1. (**F**) Example activity trace of the stimulated cell. (**G**) Example of activity traces of selected neurons. (#13 is the stimulated cell; #5 has a low coupling strength with it; #3 and #4 have a high coupling strength with it). (**H**) Linear regression plot. The coupling strength of neuron pairs was fitted as a function of the signal correlation between the pair. Regression coefficient = 143.92. P=0.0202. (**I**) A significant increase in coupling probability with increasing signal correlation to visual stimuli (P=0.003, Cochran–Armitage test for trend).

CRAOP-mediated artificial modification of neuronal response in the mouse V1 cortex

Building upon its demonstrated efficacy in mapping neuronal connectivity, our system extends its capabilities to manipulate neuronal activity, thereby enabling targeted perturbations within the neural network. To demonstrate its effectiveness, our investigation focused on the V1 cortex. We aimed to investigate whether perturbing visual-responsive neurons alters the function of other non-targeted neurons from different layers. Mice were given drifting grating visual stimuli while dual-plane calcium imaging was performed in the V1 area, covering a superficial layer of neurons and a deeper layer of neurons

(Fig. 5A). Visually responsive cells were identified in both Plane 1 (130 μm below the brain surface) (Fig. 5, B to D) and Plane 2 (330 μm below the brain surface) (Fig. 5, E to G). Subsequently, selected visually responsive neurons in the deeper layer were photostimulated during visual stimuli presentation trials. Specifically, the neurons were activated when nonpreferred orientation stimuli were presented, aiming to perturb their normal visual responsiveness (Fig. 5h). Non-targeted neurons in both Plane 1 and Plane 2 exhibited a change in orientation selectivity during these trials (Fig. 5, I to N). The targeted neurons indeed exhibited increased activity after photostimulation, resulting in a change in selectivity (Fig. 5K). Additionally, some non-targeted neurons displayed altered visual responses at the photostimulation time points (Fig. 5M). Notably, the impact of the perturbation on some non-targeted neurons caused significant disparity in the time points of photostimulation and the subsequent substantial change in their activity (Fig. 5L). This may be explained by the involvement of intricate local circuits and computational processes in visual information processing within the V1 cortex (*51*). These results showcase the potential of the CRAOP system to manipulate and record neuronal activity across distinct axially separated layers. Moreover, in future studies, the integration of connectivity mapping, single-cell manipulation, and recording using the CRAOP system, along with behavioral analysis, can provide deeper insights into the local circuit architecture and cortical computation mechanisms.

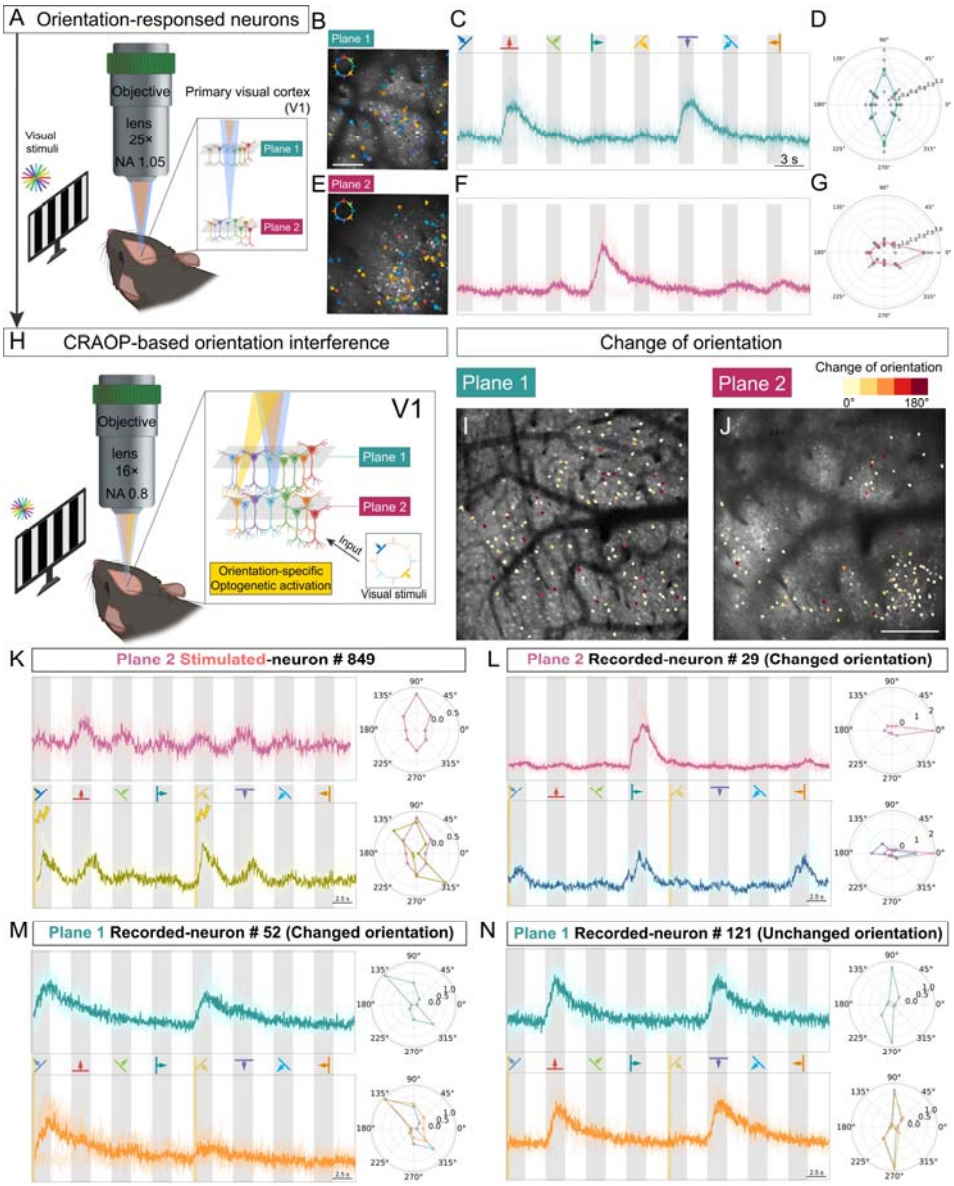

Fig. 5 Simultaneous dual-plane recording and optogenetic perturbation of mouse V1 neuronal activity during visual stimuli presentation. (**A**) Diagram of dual-plane recording under drifting grating visual stimuli. (**B**) Orientation selectivity map of plane 1 (140 μm depth). Scale bar: 100 μm. (**C** and **D**) Activity trace and corresponding polar plot of representative visual response neurons in plane 1. (**E**) Orientation selectivity map of plane 2 (240 μm depth). (**F** and **G**) Activity trace and corresponding polar plot of representative visual response neurons in plane 2. (**H**) Diagram of dual-plane recording with photostimulation under drifting grating visual stimuli. (**I** and **J**) Orientation change pattern before and after photostimulation (130 μm and 330 μm depth). Scale bar: 150 μm. (**K**) Activity trace and corresponding polar plot of the target neuron in plane 2. (**L**) Activity trace and corresponding polar plot

of a nontarget neuron in plane 2. (**M** and **N**) Activity traces and corresponding polar plots of nontarget neurons in plane 1.

Discussion

An effective strategy for achieving functional connectivity analysis involves simultaneous readout and manipulation of neuronal activity during the presentation of behavioral stimuli. While electrophysiology or optogenetics combined with calcium imaging can precisely analyze local circuits(*16*, *17*, *20*, *21*, *24*), mapping inter-layer connectivity remains necessary. In this work, we demonstrated a cross-region all-optical physiological approach with a high temporal resolution, showing the particular advantages in the dissection of inter-layer functional connectivity.

Compared to previously reported three-dimensional AOP systems(*19*, *26*, *28*, *41*), our system offers a significant advantage in terms of temporal resolution for cross-plane recording and optogenetic manipulation. In our system, spatiotemporal multiplexing(*34*–*39*) is employed to achieve simultaneous two-photon imaging of multiple focal planes within live mice, minimizing time delays among different planes (6.25 ns). This enables a more precise analysis of activity correlation between upstream and downstream neurons following optogenetic stimulation. Moreover, our system also supports simultaneous high-frame-rate imaging at different planes, making it appropriate for fast and sensitive activity indicators such as GCaMP8(*40*) and voltage sensors(*47*, *49*, *50*). In addition, the spatiotemporal multiplexing technique used to expand the imaging voxel speed limits the number of multiplexed beams by the fluorescence lifetime and the circuit demodulation capability. In addition to the visualization of neuronal activity with a high temporal resolution, our system also has the potential to benefit studies of continuous spatial dynamics of biological factors in the brain, such as the motion of glia, blood flow, and dynamic distribution of molecules within cells. Nonetheless, our results show that CRAOP is compatible with other fast axial scanning devices, such as ETL, to further promote the ability for multi-plane all-optical physiological measurement (see Figs. 2 and 3). Although CRAOP shows the capability to modify the response of neurons to sensory stimuli, there are still limitations in precisely closed-loop manipulation of behavioral output. Therefore, it is possible to improve our system by combining CRAOP with other techniques, such as anatomical analysis(*55*), large-field-of-view imaging(*32*, *56*), and more efficient neuronal manipulation like 3D-shot(*57*). Overall, our system represents a significant improvement in interrogating inter-layer connectivity with high spatial and temporal precision.

.

Reference

1. J. Lichtman, Imaging the Connectome. *Biophysical Journal*. **108**, 23a (2015).

2. L. F. Abbott, D. D. Bock, E. M. Callaway, W. Denk, C. Dulac, A. L. Fairhall, I. Fiete, K. M. Harris, M. Helmstaedter, V. Jain, N. Kasthuri, Y. LeCun, J. W. Lichtman, P. B. Littlewood, L. Luo, J. H. R. Maunsell, R. C. Reid, B. R. Rosen, G. M. Rubin, T. J. Sejnowski, H. S. Seung, K. Svoboda, D. W. Tank, D. Tsao, D. C. Van Essen, The Mind of a Mouse. *Cell*. **182**, 1372–1376 (2020).

3. H. Ko, S. B. Hofer, B. Pichler, K. A. Buchanan, P. J. Sjöström, T. D. Mrsic-Flogel, Functional specificity of local synaptic connections in neocortical networks. *Nature*. **473**, 87–91 (2011).

4. Y. Yoshimura, J. L. M. Dantzker, E. M. Callaway, Excitatory cortical neurons form fine-scale functional networks. *Nature*. **433**, 868–873 (2005).

5. S. Song, P. J. Sjöström, M. Reigl, S. Nelson, D. B. Chklovskii, Highly Nonrandom Features of Synaptic Connectivity in Local Cortical Circuits. *PLoS Biol*. **3**, e68 (2005).

6. O. A. Shemesh, D. Tanese, V. Zampini, C. Linghu, K. Piatkevich, E. Ronzitti, E. Papagiakoumou, E. S. Boyden, V. Emiliani, Temporally precise single-cell-resolution optogenetics. *Nat Neurosci*. **20**, 1796–1806 (2017).

7. P. G. Anastasiades, A. Marques-Smith, S. J. B. Butt, Studies of cortical connectivity using optical circuit mapping methods: Circuit mapping in the cerebral cortex. *J Physiol*. **596**, 145–162 (2018).

8. K. Eichler, F. Li, A. Litwin-Kumar, Y. Park, I. Andrade, C. M. Schneider-Mizell, T. Saumweber, A. Huser, C. Eschbach, B. Gerber, R. D. Fetter, J. W. Truman, C. E. Priebe, L. F. Abbott, A. S. Thum, M. Zlatic, A. Cardona, The complete connectome of a learning and memory centre in an insect brain. *Nature*. **548**, 175–182 (2017).

9. N. Kasthuri, K. J. Hayworth, D. R. Berger, R. L. Schalek, J. A. Conchello, S. Knowles-Barley, D. Lee, A. Vázquez-Reina, V. Kaynig, T. R. Jones, M. Roberts, J. L. Morgan, J. C. Tapia, H. S. Seung, W. G. Roncal, J. T. Vogelstein, R. Burns, D. L. Sussman, C. E. Priebe, H. Pfister, J. W. Lichtman, Saturated Reconstruction of a Volume of Neocortex. *Cell*. **162**, 648–661 (2015).

10. J. Winnubst, E. Bas, T. A. Ferreira, Z. Wu, M. N. Economo, P. Edson, B. J. Arthur, C. Bruns, K. Rokicki, D. Schauder, D. J. Olbris, S. D. Murphy, D. G. Ackerman, C. Arshadi, P. Baldwin, R. Blake, A. Elsayed, M. Hasan, D. Ramirez, B. Dos Santos, M. Weldon, A. Zafar, J. T. Dudman, C. R. Gerfen, A. W. Hantman, W. Korff, S. M. Sternson, N. Spruston, K. Svoboda, J. Chandrashekar, Reconstruction of 1,000 Projection Neurons Reveals New Cell

Types and Organization of Long-Range Connectivity in the Mouse Brain. *Cell*. **179**, 268-281.e13 (2019).

11. Z. Zheng, J. S. Lauritzen, E. Perlman, C. G. Robinson, M. Nichols, D. Milkie, O. Torrens, J. Price, C. B. Fisher, N. Sharifi, S. A. Calle-Schuler, L. Kmecova, I. J. Ali, B. Karsh, E. T. Trautman, J. A. Bogovic, P. Hanslovsky, G. S. X. E. Jefferis, M. Kazhdan, K. Khairy, S. Saalfeld, R. D. Fetter, D. D. Bock, A Complete Electron Microscopy Volume of the Brain of Adult Drosophila melanogaster. *Cell*. **174**, 730-743.e22 (2018).

12. W.-C. A. Lee, V. Bonin, M. Reed, B. J. Graham, G. Hood, K. Glattfelder, R. C. Reid, Anatomy and function of an excitatory network in the visual cortex. *Nature*. **532**, 370–374 (2016).

13. Z. Ding, P. G. Fahey, S. Papadopoulos, E. Y. Wang, B. Celii, C. Papadopoulos, A. B. Kunin, A. Chang, J. Fu, Z. Ding, S. Patel, K. Ponder, T. Muhammad, J. A. Bae, A. L. Bodor, D. Brittain, J. Buchanan, D. J. Bumbarger, M. A. Castro, E. Cobos, S. Dorkenwald, L. Elabbady, A. Halageri, Z. Jia, C. Jordan, D. Kapner, N. Kemnitz, S. Kinn, K. Lee, K. Li, R. Lu, T. Macrina, G. Mahalingam, E. Mitchell, S. S. Mondal, S. Mu, B. Nehoran, S. Popovych, C. M. Schneider-Mizell, W. Silversmith, M. Takeno, R. Torres, N. L. Turner, W. Wong, J. Wu, W. Yin, S. Yu, E. Froudarakis, F. Sinz, H. S. Seung, F. Collman, N. M. Da Costa, R. C. Reid, E. Y. Walker, X. Pitkow, J. Reimer, A. S. Tolias, "Functional connectomics reveals general wiring rule in mouse visual cortex" (preprint, Neuroscience, 2023), , doi:10.1101/2023.03.13.531369.

14. J. W. Lichtman, S. J. Smith, Seeing Circuits Assemble. *Neuron*. **60**, 441–448 (2008).

15. V. Emiliani, A. E. Cohen, K. Deisseroth, M. Häusser, All-Optical Interrogation of Neural Circuits. *J. Neurosci.* **35**, 13917–13926 (2015).

16. A. M. Packer, L. E. Russell, H. W. P. Dalgleish, M. Häusser, Simultaneous all-optical manipulation and recording of neural circuit activity with cellular resolution in vivo. *Nat Methods*. **12**, 140–146 (2014).

17. J. H. Marshel, Y. S. Kim, T. A. Machado, S. Quirin, B. Benson, J. Kadmon, C. Raja, A. Chibukhchyan, C. Ramakrishnan, M. Inoue, J. C. Shane, D. J. McKnight, S. Yoshizawa, H. E. Kato, S. Ganguli, K. Deisseroth, Cortical layer–specific critical dynamics triggering perception. *Science*. **365**, eaaw5202 (2019).

18. L. Carrillo-Reid, W. Yang, Y. Bando, D. S. Peterka, R. Yuste, Imprinting and recalling cortical ensembles. *Science*. **353**, 691–694 (2016).

19. A. R. Mardinly, I. A. Oldenburg, N. C. Pégard, S. Sridharan, E. H. Lyall, K. Chesnov, S. G. Brohawn, L. Waller, H. Adesnik, Precise multimodal optical control of neural ensemble activity. *Nat Neurosci*. **21**, 881–893 (2018).

20. L. Carrillo-Reid, S. Han, W. Yang, A. Akrouh, R. Yuste, Controlling Visually Guided Behavior by Holographic Recalling of Cortical Ensembles. *Cell*. **178**, 447-457.e5 (2019).

21. L. Z. Fan, S. Kheifets, U. L. Böhm, H. Wu, K. D. Piatkevich, M. E. Xie, V. Parot, Y. Ha, K. E. Evans, E. S. Boyden, A. E. Takesian, A. E. Cohen, All-Optical Electrophysiology Reveals the Role of Lateral Inhibition in Sensory Processing in Cortical Layer 1. *Cell*. **180**, 521-535.e18 (2020).

22. J. P. Rickgauer, K. Deisseroth, D. W. Tank, Simultaneous cellular-resolution optical perturbation and imaging of place cell firing fields. *Nat Neurosci*. **17**, 1816–24 (2014).

23. W. Yang, L. Carrillo-Reid, Y. Bando, D. S. Peterka, R. Yuste, Simultaneous two-photon imaging and two-photon optogenetics of cortical circuits in three dimensions. *eLife*. **7** (2018), doi:10.7554/eLife.32671.

24. Z. Zhang, L. E. Russell, A. M. Packer, O. M. Gauld, M. Häusser, Closed-loop all-optical interrogation of neural circuits in vivo. *Nat Methods*. **15**, 1037–1040 (2018).

25. K. Daie, K. Svoboda, S. Druckmann, Targeted photostimulation uncovers circuit motifs supporting short-term memory. *Nat Neurosci*. **24**, 259–265 (2021).

26. M. Dal Maschio, J. C. Donovan, T. O. Helmbrecht, H. Baier, Linking Neurons to Network Function and Behavior by Two-Photon Holographic Optogenetics and Volumetric Imaging. *Neuron*. **94**, 774-789.e5 (2017).

27. L. E. Russell, H. W. P. Dalgleish, R. Nutbrown, O. M. Gauld, D. Herrmann, M. Fişek, A. M. Packer, M. Häusser, All-optical interrogation of neural circuits in behaving mice. *Nat Protoc*. **17**, 1579–1620 (2022).

28. W. Yang, L. Carrillo-Reid, Y. Bando, D. S. Peterka, R. Yuste, Simultaneous two-photon imaging and two-photon optogenetics of cortical circuits in three dimensions. *eLife*. **7**, e32671 (2018).

29. G. L. B. Spampinato, E. Ronzitti, V. Zampini, U. Ferrari, F. Trapani, H. Khabou, A. Agraval, D. Dalkara, S. Picaud, E. Papagiakoumou, O. Marre, V. Emiliani, All-optical inter-layers functional connectivity investigation in the mouse retina. *Cell Reports Methods*. **2**, 100268 (2022).

30. B. F. Grewe, F. F. Voigt, M. van ’t Hoff, F. Helmchen, Fast two-layer two-photon imaging of neuronal cell populations using an electrically tunable lens. *Biomed. Opt. Express*. **2**, 2035–2046 (2011).

31. W. J. Shain, N. A. Vickers, B. B. Goldberg, T. Bifano, J. Mertz, Extended depth-of-field microscopy with a high-speed deformable mirror. *Opt. Lett.* **42**, 995–998 (2017).

32. N. J. Sofroniew, D. Flickinger, J. King, K. Svoboda, A large field of view two-photon mesoscope with subcellular resolution for in vivo imaging. *eLife*. **5** (2016), doi:10.7554/eLife.14472.

33. L. Kong, J. Tang, J. P. Little, Y. Yu, T. Lämmermann, C. P. Lin, R. N. Germain, M. Cui, Continuous volumetric imaging via an optical phase-locked ultrasound lens. *Nat. Methods*. **12**, 759–762 (2015).

34. W. Amir, R. Carriles, E. E. Hoover, T. A. Planchon, C. G. Durfee, J. A. Squier, Simultaneous imaging of multiple focal planes using a two-photon scanning microscope. *Opt. Lett.* **32**, 1731–1733 (2007).

35. A. Cheng, J. T. Gonçalves, P. Golshani, K. Arisaka, C. Portera-Cailliau, Simultaneous two-photon calcium imaging at different depths with spatiotemporal multiplexing. *Nat Methods*. **8**, 139–142 (2011).

36. J. L. Chen, F. F. Voigt, M. Javadzadeh, R. Krueppel, F. Helmchen, Long-range population dynamics of anatomically defined neocortical networks. *eLife*. **5** (2016), doi:10.7554/eLife.14679.

37. D. R. Beaulieu, I. G. Davison, K. Kilic, T. G. Bifano, J. Mertz, Simultaneous multiplane imaging with reverberation two-photon microscopy. *Nat Methods*. **17**, 283–286 (2020).

38. J. Demas, J. Manley, F. Tejera, K. Barber, H. Kim, F. M. Traub, B. Chen, A. Vaziri, High-speed, cortex-wide volumetric recording of neuroactivity at cellular resolution using light beads microscopy. *Nat Methods*. **18**, 1103–1111 (2021).

39. C. H. Yu, J. N. Stirman, Y. Yu, R. Hira, S. L. Smith, Diesel2p mesoscope with dual independent scan engines for flexible capture of dynamics in distributed neural circuitry. *Nat Commun*. **12**, 6639 (2021).

40. Y. Zhang, M. Rózsa, Y. Liang, D. Bushey, Z. Wei, J. Zheng, D. Reep, G. J. Broussard, A. Tsang, G. Tsegaye, S. Narayan, C. J. Obara, J.-X. Lim, R. Patel, R. Zhang, M. B. Ahrens, G. C. Turner, S. S.-H. Wang, W. L. Korff, E. R. Schreiter, K. Svoboda, J. P. Hasseman, I. Kolb, L. L. Looger, Fast and sensitive GCaMP calcium indicators for imaging neural populations. *Nature*. **615**, 884–891 (2023).

41. C. Huang, C.-Y. Tai, K.-P. Yang, W.-K. Chang, K.-J. Hsu, C.-C. Hsiao, S.-C. Wu, Y.-Y. Lin, A.-S. Chiang, S.-W. Chu, All-Optical Volumetric Physiology for Connectomics in Dense Neuronal Structures. *iScience*. **22**, 133–146 (2019).

42. Kolb, Ilya, Hasseman, Jeremy, Tsegaye, Getahun, Tsang, Arthur, Reep, Daniel, Zheng, Jihong, Arthur, Ben, Marvin, Jonathan S., Svoboda, Karel, L Looger, Loren, Korff, Wyatt, Team, GENIE Project, Optimization of genetically encoded GABA indicator (2022), p. 1367523 Bytes, , doi:10.25378/JANELIA.19709311.V2.

43. H. Adesnik, A. Naka, Cracking the Function of Layers in the Sensory Cortex. *Neuron*. **100**, 1028–1043 (2018).

44. S. Nagayama, R. Homma, F. Imamura, Neuronal organization of olfactory bulb circuits. *Frontiers in Neural Circuits*. **8** (2014).

45. R. Miles, R. K. Wong, Excitatory synaptic interactions between CA3 neurones in the guinea-pig hippocampus. *The Journal of Physiology*. **373**, 397–418 (1986).

46. S. J. Guzman, A. Schlögl, M. Frotscher, P. Jonas, Synaptic mechanisms of pattern completion in the hippocampal CA3 network. *Science*. **353**, 1117–1123 (2016).

47. Z. Liu, X. Lu, V. Villette, Y. Gou, K. L. Colbert, S. Lai, S. Guan, M. A. Land, J. Lee, T. Assefa, D. R. Zollinger, M. M. Korympidou, A. L. Vlasits, M. M. Pang, S. Su, C. Cai, E. Froudarakis, N. Zhou, S. S. Patel, C. L. Smith, A. Ayon, P. Bizouard, J. Bradley, K. Franke, T. R. Clandinin, A. Giovannucci, A. S. Tolias, J. Reimer, S. Dieudonné, F. St-Pierre, Sustained deep-tissue voltage recording using a fast indicator evolved for two-photon microscopy. *Cell*. **185**, 3408-3425.e29 (2022).

48. O. Yizhar, L. E. Fenno, M. Prigge, F. Schneider, T. J. Davidson, D. J. O'Shea, V. S. Sohal, I. Goshen, J. Finkelstein, J. T. Paz, K. Stehfest, R. Fudim, C. Ramakrishnan, J. R. Huguenard, P. Hegemann, K. Deisseroth, Neocortical excitation/inhibition balance in information processing and social dysfunction. *Nature*. **477**, 171–178 (2011).

49. D. S. Peterka, H. Takahashi, R. Yuste, Imaging Voltage in Neurons. *Neuron*. **69**, 9–21 (2011).

50. N. Vogt, Voltage sensors: challenging, but with potential. *Nat Methods*. **12**, 921–924 (2015).

51. L. Cossell, M. F. Iacaruso, D. R. Muir, R. Houlton, E. N. Sader, H. Ko, S. B. Hofer, T. D. Mrsic-Flogel, Functional organization of excitatory synaptic strength in primary visual cortex. *Nature*. **518**, 399–403 (2015).

52. A. Wertz, S. Trenholm, K. Yonehara, D. Hillier, Z. Raics, M. Leinweber, G. Szalay, A. Ghanem, G. Keller, B. Rózsa, K.-K. Conzelmann, B. Roska, Single-cell–initiated monosynaptic tracing reveals layer-specific cortical network modules. *Science*. **349**, 70–74 (2015).

53. L. F. Rossi, K. D. Harris, M. Carandini, Spatial connectivity matches direction selectivity in visual cortex. *Nature*. **588**, 648–652 (2020).

54. K. E. Kishi, Y. S. Kim, M. Fukuda, M. Inoue, T. Kusakizako, P. Y. Wang, C. Ramakrishnan, E. F. X. Byrne, E. Thadhani, J. M. Paggi, T. E. Matsui, K. Yamashita, T. Nagata, M. Konno, S. Quirin, M. Lo, T. Benster, T. Uemura, K. Liu, M. Shibata, N. Nomura, S. Iwata, O. Nureki, R. O. Dror, K. Inoue, K. Deisseroth, H. E. Kato, Structural basis for channel conduction in the pump-like channelrhodopsin ChRmine. *Cell*. **185**, 672-689.e23 (2022).

55. The MICrONS Consortium, J. A. Bae, M. Baptiste, C. A. Bishop, A. L. Bodor, D. Brittain, J. Buchanan, D. J. Bumbarger, M. A. Castro, B. Celii, E. Cobos, F. Collman, N. M. Da Costa, S. Dorkenwald, L. Elabbady, P. G. Fahey, T. Fliss, E. Froudarakis, J. Gager, C. Gamlin, W. Gray-Roncal, A. Halageri, J. Hebditch, Z. Jia, E. Joyce, J. Joyce, C. Jordan, D. Kapner, N. Kemnitz, S. Kinn, L. M. Kitchell, S. Koolman, K. Kuehner, K. Lee, K. Li, R. Lu, T. Macrina, G. Mahalingam, J. Matelsky, S. McReynolds, E. Miranda, E. Mitchell, S. S. Mondal, M. Moore, S. Mu, T. Muhammad, B. Nehoran, O. Ogedengbe, C. Papadopoulos, S. Papadopoulos, S. Patel, X. Pitkow, S. Popovych, A. Ramos, R. Clay Reid, J. Reimer, P. K. Rivlin, V. Rose, C. M. Schneider-Mizell, H. S. Seung, B. Silverman, W. Silversmith, A. Sterling, F. H. Sinz, C. L. Smith, S. Suckow, M. Takeno, Z. H. Tan, A. S. Tolias, R. Torres, N. L. Turner, E. Y. Walker, T. Wang, A. Wanner, B. A. Wester, G. Williams, S. Williams, K. Willie, R. Willie, W. Wong, J. Wu, C. Xu, R. Yang, D. Yatsenko, F. Ye, W. Yin, R. Young, S. Yu, D. Xenes, C. Zhang, "Functional connectomics spanning multiple areas of mouse visual cortex" (preprint, Neuroscience, 2021), , doi:10.1101/2021.07.28.454025.

56. T. H. Kim, Y. Zhang, J. Lecoq, J. C. Jung, J. Li, H. Zeng, C. M. Niell, M. J. Schnitzer, Long-Term Optical Access to an Estimated One Million Neurons in the Live Mouse Cortex. *Cell Reports*. **17**, 3385–3394 (2016).

57. N. C. Pégard, A. R. Mardinly, I. A. Oldenburg, S. Sridharan, L. Waller, H. Adesnik, Three-dimensional scanless holographic optogenetics with temporal focusing (3D-SHOT). *Nat Commun*. **8**, 1228 (2017).

58. T. A. Pologruto, B. L. Sabatini, K. Svoboda, ScanImage: Flexible software for operating laser scanning microscopes. *BioMedical Engineering OnLine*. **2**, 13 (2003).

59. S. Xiao, J. Mertz, Contrast improvement in two-photon microscopy with instantaneous differential aberration imaging. *Biomed Opt Express*. **10**, 2467–2477 (2019).

60. K. M. Hagihara, T. Murakami, T. Yoshida, Y. Tagawa, K. Ohki, Neuronal activity is not required for the initial formation and maturation of visual selectivity. *Nat Neurosci*. **18**, 1780–8 (2015).

61. H. Dana, T.-W. Chen, A. Hu, B. C. Shields, C. Guo, L. L. Looger, D. S. Kim, K. Svoboda, Thy1-GCaMP6 Transgenic Mice for Neuronal Population Imaging In Vivo. *PLoS ONE*. **9**, e108697 (2014).

62. T. L. Daigle, L. Madisen, T. A. Hage, M. T. Valley, U. Knoblich, R. S. Larsen, M. M. Takeno, L. Huang, H. Gu, R. Larsen, M. Mills, A. Bosma-Moody, L. A. Siverts, M. Walker, L. T. Graybuck, Z. Yao, O. Fong, T. N. Nguyen, E. Garren, G. H. Lenz, M. Chavarha, J. Pendergraft, J. Harrington, K. E. Hirokawa, J. A. Harris, P. R. Nicovich, M. J. McGraw, D. R. Ollerenshaw, K. A. Smith, C. A. Baker, J. T. Ting, S. M. Sunkin, J. Lecoq, M. Z. Lin, E. S. Boyden, G. J. Murphy, N. M. Da Costa, J. Waters, L. Li, B. Tasic, H. Zeng, A Suite of Transgenic Driver and Reporter Mouse Lines with Enhanced Brain-Cell-Type Targeting and Functionality. *Cell*. **174**, 465-480.e22 (2018).

63. J. Z. Tsien, D. F. Chen, D. Gerber, C. Tom, E. H. Mercer, D. J. Anderson, M. Mayford, E. R. Kandel, S. Tonegawa, Subregion- and Cell Type–Restricted Gene Knockout in Mouse Brain. *Cell*. **87**, 1317–1326 (1996).

64. C. Sun, W. Yang, J. Martin, S. Tonegawa, Hippocampal neurons represent events as transferable units of experience. *Nat Neurosci*. **23**, 651–663 (2020).

65. Y. Wang, D. Zhu, B. Liu, K. D. Piatkevich, Craniotomy Procedure for Visualizing Neuronal Activities in Hippocampus of Behaving Mice. *JoVE*, 62266 (2021).

66. A. F. Ulivi, T. P. Castello-Waldow, G. Weston, L. Yan, R. Yasuda, A. Chen, A. Attardo, Longitudinal Two-Photon Imaging of Dorsal Hippocampal CA1 in Live Mice. *JoVE*, 59598 (2019).

67. M. Pachitariu, C. Stringer, M. Dipoppa, S. Schröder, L. F. Rossi, H. Dalgleish, M. Carandini, K. D. Harris, Suite2p: beyond 10,000 neurons with standard two-photon microscopy. *bioRxiv*, 061507 (2017).

Materials and Methods

Optical setup of the CRAOP system

The detailed system setup is demonstrated in fig.S1. The system is composed of a pulsed femto second laser (80 MHz, Chameleon Discovery, Coherent) which has two outputs and a custom-built two-photon laser scanning module. The imaging laser which has a build-in dispersion compensation module is tuned to 920 nm for calcium imaging. The stimuli laser is fixed to 1040 nm to perform two-photon optogenetics stimulation. The imaging laser power is controlled with a Pockels cell (Pockels cell: 350-80-LA, Controller: 302RM, Conoptics, Inc.). After the Pockels cell, a half wave plate (AHWP05M-980, Thorlabs) mounted on an electric rotation stage (PRM1/MZ8, Thorlabs) and a polarization beam splitter (PBS203, Thorlabs) are introduced into the optical path to realize adjustment of energy distribution between two imaging planes. The lower plane imaging path is ~1.8 m shorter than the upper plane imaging path which leads to ~6.25 ns delay between two beamlets. The upper plane imaging path goes through a 2X beam expander composed of two achromats (AC254-75-B and AC254-150-B, Thorlabs, not shown in the figure) to improve axial resolution. An offset achromat (AC254-75-B, Thorlabs), an ETL (EL-16-40-TC, Optotune), and two other achromats (AC254-200-B and AC254-100-B, Thorlabs) are placed at different intervals to obtain designed focal power bias. The lower plane imaging beam and upper plane imaging beam are combined with another polarization beam splitter (CCM1-PBS253/M, Thorlabs). A 6-mm galvanometric scan mirror (8315K, Cambridge Technology) and an 8 kHz Resonant mirror (CRS 8 kHz, Cambridge Technology) lead to 60Hz imaging framerate at 256×256 pixel number. The combined beam is then imaged to the objective (16X CFI75 LWD, NA 0.80, Nikon) pupil by the combination of a scan lens (SL50-2P2, Thorlabs) and a tube lens (TL200-CLS2, Thorlabs). The objective is mounted on a piezo stage (P-725.4CD, Physik Instrumente) to perform long-range Z-scanning. A three-dimensional (3D) high-precision motor stage (Stage: M-VP-25XA-XYZL, Controller: ESP301, Newport) is used to move the sample relative to the objective.

In the 1040 nm photostimulation path, another Pockels cell (Pockels cell: 350-80-LA, Controller: 302RM, Conoptics, Inc.) is used to modulate the photostimulation power. A X-Y 2-axis galvanometric scan mirror (8315K, Cambridge Technology) steers the beam to perform a serial spiral scan of neurons. After a scan lens (SL50-2P2, Thorlabs), the stimuli beam is combined with the imaging beam by a dichroic mirror (DMSP1000R, Thorlabs).

The fluorescence signal is separated from the main excitation path by a dichroic mirror (DMLP805R, Thorlabs). A collection lens pair (#49-284, Edmund; KPA034-C, Newport) collects as much possible photons to enhance system efficiency. Another dichroic mirror (FF560-Di01-35.5x50.0, Sermock) split the emission light into two channels in which red (FF01-632/148-29-D, Sermock) and green (FF03-525/50-30-D, Sermock) fluorescence emission

filters are located. Photomultiplier tubes (H10770PA-40, Hamamatsu) are used to detect emission light. The detection arm design is mainly based on MIMMS (Janelia Farm Research Campus). The system is controlled by scanimage (vidiro) software(*58*).

We replaced the offset achromat (AC254-75-B, Thorlabs) with another achromat (AC254-250-B, Thorlabs) in the experiment with the axial interval between two planes less than 300 microns.

Signal demultiplexing of the CRAOP system

The wiring diagram of the data acquisition system is demonstrated in Fig. S3A. A high-speed transimpedance amplifier (DHPCA-100, Femto) amplifies current signals from PMT and sends voltage signals for subsequent demultiplexing. After amplification and filtering, fluorescence signals are split into two channels by a power splitter (ZAPD-30-S+, MiniCircuits)(*59*). A longer BNC cable (~1.3 m) delays one of the channels relative to another by 6.25 ns. We then synchronize the data sampling clock of the data acquisition board (vDAQ data acquisition hardware, vidiro) to the clock pulse train generated by femto second laser. To sample each channel at the peak of the signals, the laser clock phase is also adjusted by altering the length of the BNC cable according to the intensity of the image. Thus, the peak of fluorescence signal pulse emitting from the lower plane is captured at channel 1. Accordingly, the peak of the fluorescence signal pulse emitting from the upper plane is captured at channel 2. The bandwidth of the transimpedance amplifier can be adjusted to strike a balance between signal-to-noise ratio and signal aliasing (Fig. S4). The remaining signal mixing between two channels can be solved by linear demixing(*36*) (fig.S5).

Spatial resolution calibration of the CRAOP system

The experimental resolution of the microscope is evaluated by measuring the excitation point spread function (PSFex) as the full width at half-maximum (FWHM) of the imaging intensity profile of 0.51 μm green fluorescent polymer microspheres (Fluoro-Max, Dia: 0.51 μm, Thermo Fisher Scientific) buried in 2% agarose gel. Cross sections of green fluorescent polymer microspheres are also illustrated in Fig. 1.

Optogenetics calibration of CRAOP system

Since the opening of the opsin ion channel is a cumulative effect, and the axonal dendrites adjacent to the soma may also be located in the path of the excitation light, even the soma that is not located in the precise focal point still has a certain probability of being activated. Stray light or poor target selection can also contribute to this neighboring associated excitation. To evaluate this putative ‘off-target’ stimulation from our optogenetics manipulation, we quantify the relative response of opsin-expressed neurons with different targeted location. Ten seconds of data pre-stimulus is used to calculate the

baseline value. The maximum response of two seconds of data after optogenetic stimulus is used to calculate the ΔF/F. The stimulus patterns are spaced away from the soma at certain intervals (fig. S2A). The data from cells (N = 4) are finally normalized to the mean value of the excitation peaks of each cell (fig. S2B). Measurement results show that photostimulation in our system has high lateral resolution. Axial 'off target' stimulation is also measured. ΔF/F response is calculated from cells (N = 4) and normalized to the mean value of the excitation peaks of each cell when photostimulation focus is at the same axial position with the imaging beam (fig. S2C).

Visual stimuli setup and analysis

A liquid crystal display monitor with 1920×1080-pixel resolution is placed 15 cm away from the mouse's eyes. The front of the screen is covered with a blue filter film to reduce visual stimuli light getting into PMT. We generated drifting sine wave gratings in different directions (0,45,90,135,180,225,270,315 degrees, 5 trials) by custom software in Psychtoolbox running on MATLAB. Each direction of drifting grating last 2 s and uniform gray was displayed between different directions of drifting gratings. To further reduce screen light pollution, the screen display was set to blue only. The monitor is controlled by another computer. The synchronization of visual stimuli and two-photon imaging is achieved by counting the frame trigger with a NI USB6008 DAQ card. The orientation selectivity index (OSI) is calculated as (response to preferred direction − averaged response to two orthogonal directions) / (response to preferred orientation + averaged response to two orthogonal directions)(*60*). In Fig. S10, the visual stimuli were replaced by presentations of cartoon video clips on the display monitor described above.

Animals

All experimental procedures were approved by the Institutional Animal Care and Use Committee (IACUC) of Tsinghua University and were performed using the principles outlined in the Guide for the Care and Use of Laboratory Animals of Tsinghua University. All C57BL/6J mice were maintained under standard conditions by the Animal Research Center of Tsinghua University. Thy1-GCaMP6s(*61*) (stock number # 024275), Ai162(*62*)(TIT2L-GC6s-ICL-tTA2)-D mice (stock number # 031562) and Camk2a-cre(*63*) (stock number # 005359) mice were obtained from The Jackson Laboratory. Transgenic mice were genotyped through PCR using genomic DNA and Jackson Laboratories-provided primers.

Viral constructs

The viral constructs used in the experiment were stored at -80°C until use after being subdivided into aliquots. For calcium imaging and optogenetics in CA1, a mixture of $AAV_{2/9}$-CaMKIIα-ERCreER (OBiO), $AAV_{2/9}$-EF1α-DIO-ChRmine-mScarlet (OBiO), and $AAV_{2/9}$-NES-GCaMP8m

(Taitool) was prepared. For calcium imaging and optogenetics in CA3, a mixture of $AAV_{2/9}$-CaMKIIα-ERCreER (OBiO) and $AAV_{2/9}$-EF1α-DIO-ChRmine-mScarlet (OBiO) was prepared. For calcium imaging and optogenetics in the cortex, $AAV_{2/9}$-hSyn-C1V1(E122T/E162T)-TS-mCherry or $AAV_{2/9}$-hSyn-NES-GCaMP8m-p2A-rsChRmine (Taitool) was used. For voltage imaging, a mixture of $AAV_{2/9}$-CaMKIIα-Cre (OBiO), $AAV_{2/9}$-EF1α-DIO-JEDI-2P-Kv (OBiO), and $AAV_{2/9}$-CaMKIIα-C1V1(t/t)-ER2 (Taitool) was prepared. For GABA imaging, a mixture of $AAV_{2/9}$-CaMKIIα-Cre and $AAV_{2/9}$-EF1α-DIO-iGABAsnFR2 was prepared. The viral concentration of all viruses in the mixture was adjusted to 1-2 × 10^{12} viral genomes (v.g.)/ml by adding a buffer (PBS 1× with 5% glycerol).

Surgery procedures

Hippocampus surgery

For virus injections into the hippocampus, mice were first anesthetized with Avertin (0.3g/kg body weight). Craniotomies on the skull over the right hippocampus were performed using a 0.5 mm-diameter drill, and 300 nl of the virus was injected into the dorsal CA1 (-2.0 mm A/P, -1.5 mm M/L, and −1.4 mm D/V) or CA3 (-2.7 mm A/P, -2.0 mm M/L, and −1.9 mm D/V) using a 10 μl nanofil syringe controlled by UMP3 and Micro4 system (WPI) with a speed of 60 nl/min. After the injection, the needle remained in place for 10 min to ensure that the virus spread to the targeted area before it was slowly withdrawn. After injection, mice were returned to their home cages and were allowed to recover for at least 5 days before performing further experiments.

Imaging window implantation was performed 5 days to 14 days after the virus injection. Anesthesia was induced with 5% isoflurane before surgery and was kept with 1.5% isoflurane during the surgery. Prior to surgery, mice were administered an anti-inflammatory drug Meloxicam (8 mg/kg) subcutaneously. A 3 mm-diameter craniotomy was made using a micro-drill at the AAV injection site. The cortex tissue above the hippocampus was aspirated with a 27-gauge needle connected to a pump until the fibers of the corpus callosum became visible, exposing the alveus of the hippocampus(*64–66*). A stainless-steel cannula (3 mm diameter, 1.6 mm height) covered by a cover glass (3 mm diameter, 0.17 mm thickness) was inserted into the opening until the glass was in contact with the fibers. The cannula was secured in place with glue and dental cement, and a stainless-steel head-post was also fixed onto the skull using dental cement. Following surgery, mice were returned to their home cages and were monitored daily. Meloxicam (4 mg/kg/day) was given subcutaneously for 3 consecutive days after surgery to prevent inflammation.

Mice were allowed to recover for at least 3 weeks before imaging experiments were performed.

Cortex surgery

For mouse cortex imaging experiments in Fig.1, Fig.2, and Fig.5, double transgenic Ai162/ Camk2a-cre mice were used. AAV-hSyn-C1V1(E122T/E162T)-TS-mCherry virus was injected into the targeted area. An amount of 300 nl of the virus was injected to layer 2/3 (~250 μm deep) and layer 5 (~500 μm deep) of the S1 (-1 mm A/P and -3 mm M/L) or V1 (-4 mm A/P and -3 mm M/L) of the mouse cortex 3 weeks prior to the craniotomy surgery. The virus was front-loaded into the beveled glass pipette and injected at a rate of 50 ~ 80 nL/min. After the injection, the needle remained in place for 10 min to ensure that the virus spread to the targeted area before it was slowly withdrawn. Craniotomy surgery was performed by drilling a 3 mm-diameter opening in the skull centered at the injection site. A circular glass coverslip was placed and sealed using a cyanoacrylate adhesive, and a stainless-steel head-post was fixed onto the skull using dental cement.

For experiments in Fig.4, C57BL/6J mice were used. First, a cranial opening was performed as described above and then $AAV_{2/9}$-hSyn-NES-GCaMP8m-p2A-rsChRmine virus was injected into the V1 area (-4 mm A/P and -3 mm M/L). Injections were performed at a rate of 60 nl/min at 3 depths (-150 μm, -200 μm and -250 μm below the dura surface), resulting in a total amount of 600 nl virus injected. After injection at each depth, the needle remained in place for 10 min before it was slowly withdrawn. After the virus injection, the coverslip and head-post were placed and sealed as described above.

Prior to all cortex surgeries, mice were administered Meloxicam (8 mg/kg) and Dexamethasone (1 mg/kg) subcutaneously. Meloxicam (4 mg/kg/day) was also given subcutaneously for 3 consecutive days after the surgery. Mice were used in imaging experiments at least 2 weeks after the craniotomy surgeries.

Treatments on mice for imaging experiments

Sparse labeling of neurons

Tamoxifen dissolved in corn oil (5 mg/ml) was administrated to mice via intraperitoneal injection (30mg/kg body weight) 1 week before imaging. This allowed the expression of ChRmine-mScarlet in a sparse subpopulation of CA1 or CA3 neurons (for corresponding experiments in Fig.3 and Fig. S8).

Induction of seizure-like behaviors

For experiments on GABA signals, mice were injected with kainic acid (5mg/kg body weight, i.p.) before imaging. Seizure-like behaviors typically appeared 30 minutes after drug injection. Imaging was performed during the seizure-like behaviors with a supplement of 0.5% isoflurane for light anesthesia.

Anesthesia

During the majority of imaging and optogenetics experiments, mice were head-fixed and anesthetized by 1% to 1.5% isoflurane. For visual stimulation experiments, no anesthesia was given during the visual stimuli presentation. For experiments in Fig. 4 and fig. S10, mice were given an intraperitoneal injection of chlorprothixene (5 mg/kg) before head fixation for a sedative effect.

Data analysis

Calcium data analysis

For all calcium imaging data, Suite2p was used to extract spatial footprints and activity traces of putative neurons(*67*). The results were manually inspected and refined by removing ROIs that were misclassified as neurons by the software. Fluorescence fluctuations in the surrounding neuropil of each cell were subtracted from the raw fluorescence traces (coefficient 0.7), and then $\Delta F/F_0$ was calculated for each ROI. F_0 was calculated as the mean fluorescence intensity of the 10% frames with the lowest intensity. A low-pass Butterworth filter was applied to the raw extracted trace for the calcium traces displayed in the figures.

Voltage data analysis

For all voltage imaging data, the voltage signal was extracted after image registration. The ROIs are determined by the morphology of neurons in the averaged image. The Z-score algorithm is used to normalize the activity trace of neurons. The baseline is calculated as the median of the activity trace.

GABA signal data analysis

For the GABA sensor imaging data, the signal was extracted manually from selected areas in the image after image registration. The Z-score algorithm is applied to the GABA sensor signal trace. The baseline is calculated as the median of the activity trace.

Calculation of coupling strength and activity correlation

For data in Fig.4, the coupling strength of a neuron to a photostimulated neuron was calculated using the following method. First, the mean fluorescence value in a 0.5-second window after the end of the photostimulus was calculated as A_i. Next, the mean fluorescence value in a 3-second window before the onset of the photostimulus was calculated as Bi. The coupling strength for this neuron to the targeted photostimulated neuron was calculated by averaging all $S_i = A_i - B_i$ over all such stimulation trials.

To determine which neurons are presumably coupled with the targeted neuron, we made several assumptions. We assumed if the neuron pair is not coupled, the coupling strength should be sampled from a Gaussian distribution centered around zero due to stochastic fluctuations and firings. We also assume that strong negative coupling between neurons is rare. Thus, we set a threshold for detecting coupled neurons. The threshold is the absolute value of the 5th percentile of all negative coupling strength values in all trials in a mouse. If the coupling strength exceeded this threshold, we assume it is unlikely to purely result from stochasticity, and we denote the corresponding neuron pairs as coupled.

For correlation analysis, the rolling-averaged calcium traces were used to compute Pearson's correlation coefficient of a pair of neurons in a given time window. The signal correlation of neurons in V1 was calculated for the whole-time window in which visual stimuli were presented. In Fig.4, for defining low, medium and high signal correlation levels, the values 0.2 and 0.4 were used as boundaries. The noise correlation (fig. S9) was calculated for the time points in which no visual stimuli were presented (when mice were in the darkness).

Statistics

Statistical tests were performed using GraphPad Prism 9 and customized R/Python scripts. The linear regression model was used for fitting the relationship between coupling strength and signal correlation. Cochran–Armitage test for trend was used to test for the significance of a linear trend in proportions. The two-tailed Wilcoxon signed-rank test was used as a

paired difference test without the assumption of normally distributed samples. A p-value less than 0.05 was considered statistically significant. $*p < 0.05$; $**p < 0.01$; $***p < 0.001$; $****p < 0.0001$; n.s., nonsignificant ($p > 0.05$).

Acknowledgments

Funding:

This work is supported by:

STI2030-Major Projects 2022ZD0212000

National Natural Science Foundation of China (NSFC) 32021002

National Natural Science Foundation of China (NSFC) 61971265

“Bio-Brain+X” Advanced Imaging Instrument Development Seed Grant

Author contributions: Each author's contribution(s) to the paper should be listed (we suggest following the CRediT model with each CRediT role given its own line. No punctuation in the initials.

Examples:

Conceptualization: YZ, LK, BL

Methodology: CL, YH, LK, BL

Investigation: YH, CL

Visualization: CL, YH, BL

Supervision: YZ, LK, BL

Writing—original draft: CL, YH, LK, BL

Writing—review & editing: CL, YH, YZ, LK, BL

Competing interests: All authors declare no competing interests.

Data and materials availability: The data that support the findings of this study are available from the corresponding author upon reasonable request. The code used in this study is available from the corresponding author upon reasonable request.

Fig. S1.

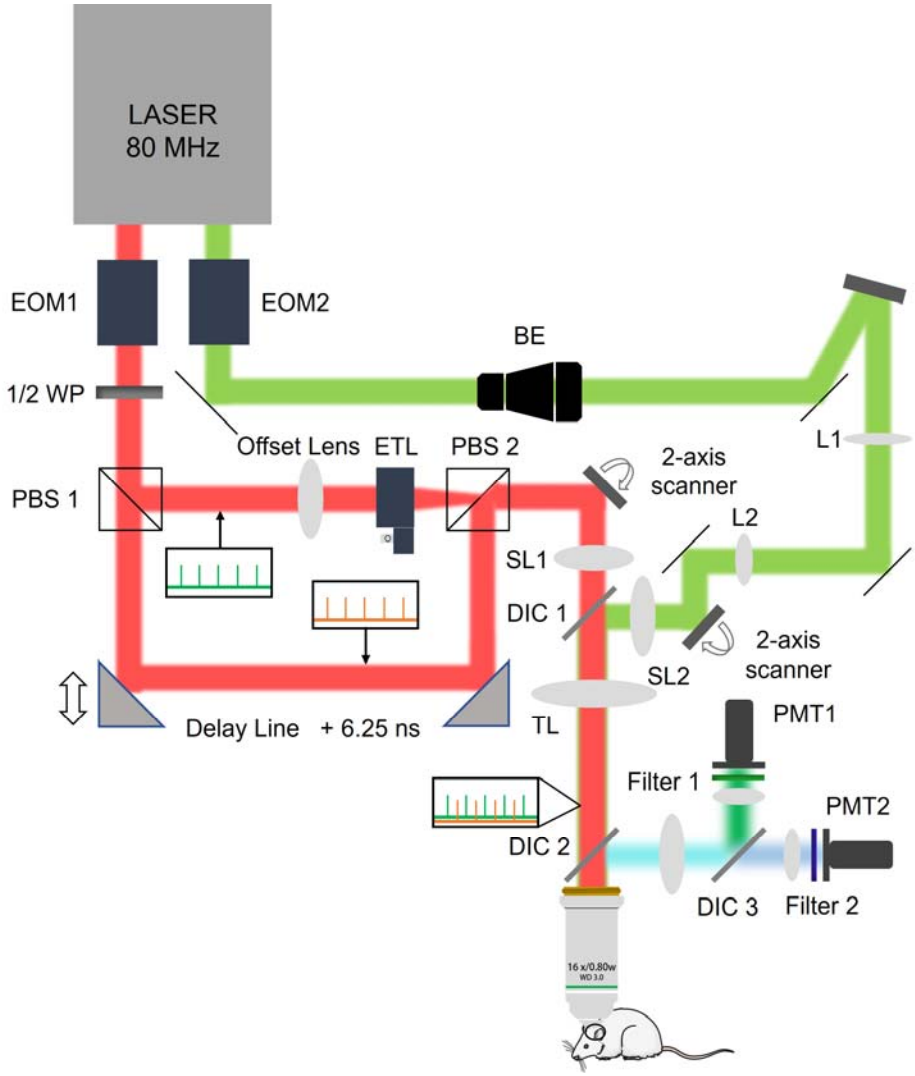

Fig. S1. Detailed optical setup of CRAOP. EOM: Electro optic modulator, 1/2 WP: Halfwave plate, PBS: Polarization beam splitter, BE: Beam expander, L: Lens, SL: Scan lens, TL: Tube lens, DIC: Dichromatic mirror.

Fig. S2.

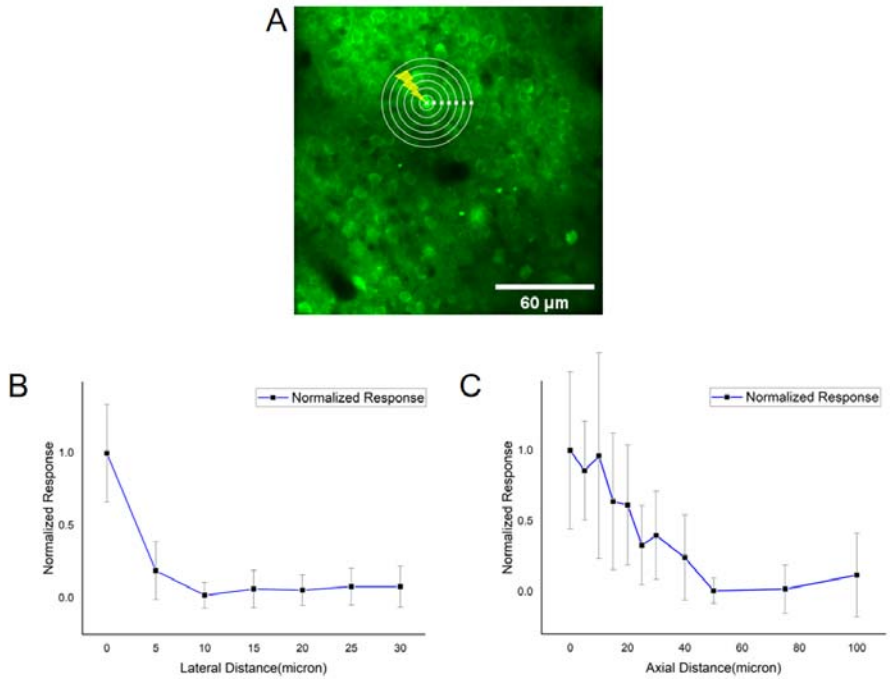

Fig. S2. Optogenetic 'off-target' properties calibration. A. Diagram of stimulation response PSF measurement. Stimulation response PSF is measured in mouse S1 cortex region. **B**. Normalized stimulation response to the photostimulation versus lateral distance between stimuli point and measured cell. ΔF/F is normalized to the averaged response of on-target stimuli. **C**. Normalized stimulation response to the photostimulation versus axial distance between stimuli point and measured cell. ΔF/F is normalized to the averaged response of on-target stimuli. Data are represented as mean ± standard deviation of the mean.

Fig. S3.

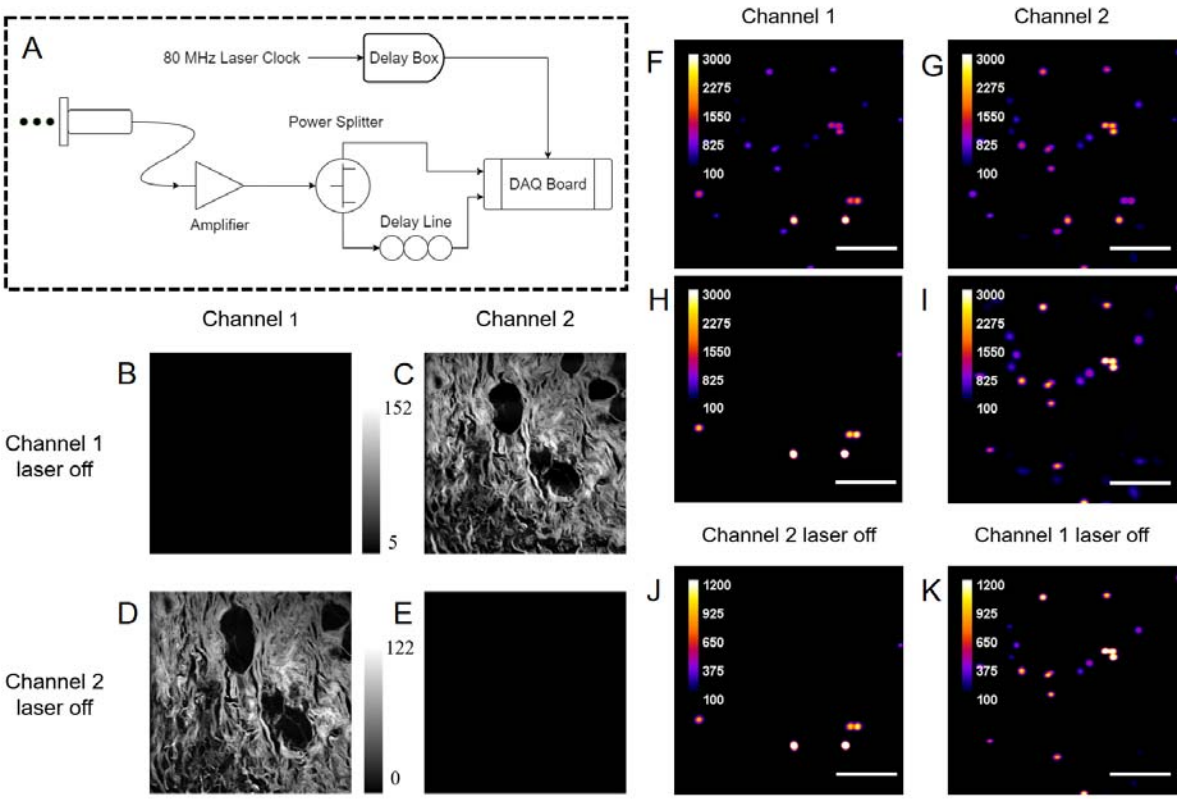

Fig. S3. Demultiplexing electronics and channel cross-talk evaluation. (**A**) Wiring diagram of data acquisition system. Two channels are delayed relatively by about 6.25 ns. (**B**). Captured Image of channel 1 when laser corresponding to channel 1 is off. (**C**) Captured Image of channel 2 when laser corresponding to channel 1 is off. (**D**) Captured Image of channel 1 when laser corresponding to channel 2 is off. (**E**) Captured Image of channel 2 when laser corresponding to channel 2 is off. (**F** and **G**) Averaged Image of channel 1,2 when both planes are excited. Scale bar: 20 μm. (**H** and **I**). Demixed Image of channel 1,2 when both planes are excited. (**J** and **K**). Channel 1,2 Image when laser corresponding to channel 2,1 is off.

Fig. S4.

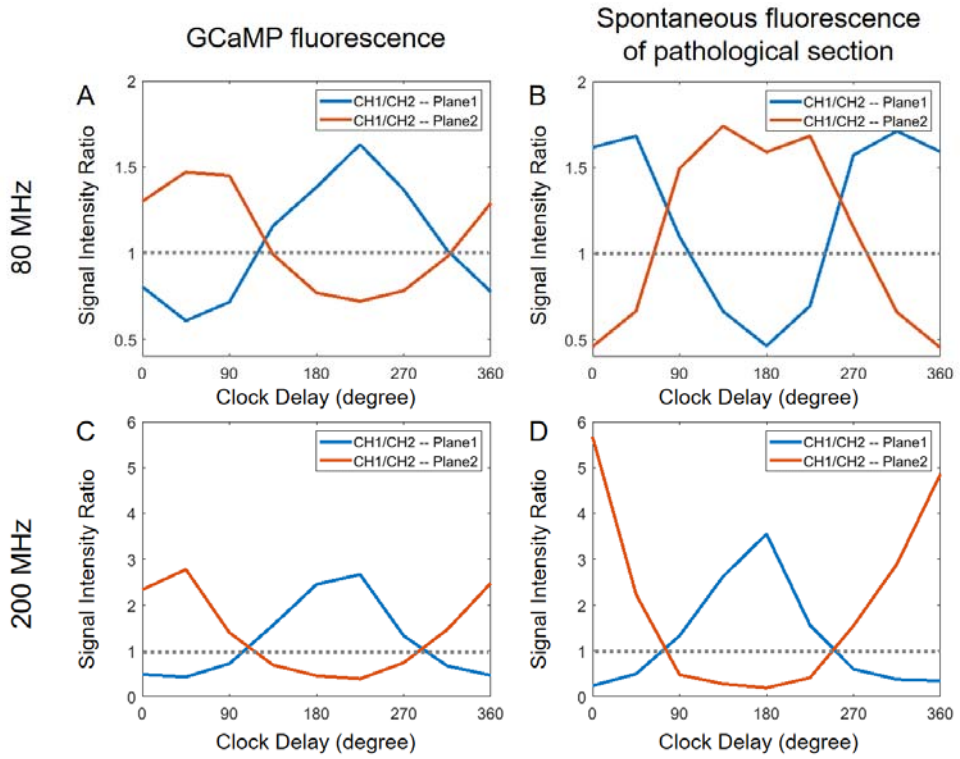

Fig. S4. Channel crosstalk between two digitalized channels with different cut-off frequencies and biological samples. (**A**) Channel crosstalk with 80 MHz cut-off frequency and GCaMP labeled neuron. (**B**) Channel crosstalk with 80 MHz cut-off frequency and H&E stained pathological section. (**C**) Channel crosstalk with 200 MHz cut-off frequency and GCaMP labeled neuron. (**D**) Channel crosstalk with 200 MHz cut-off frequency and H&E stained pathological section.

Fig. S5.

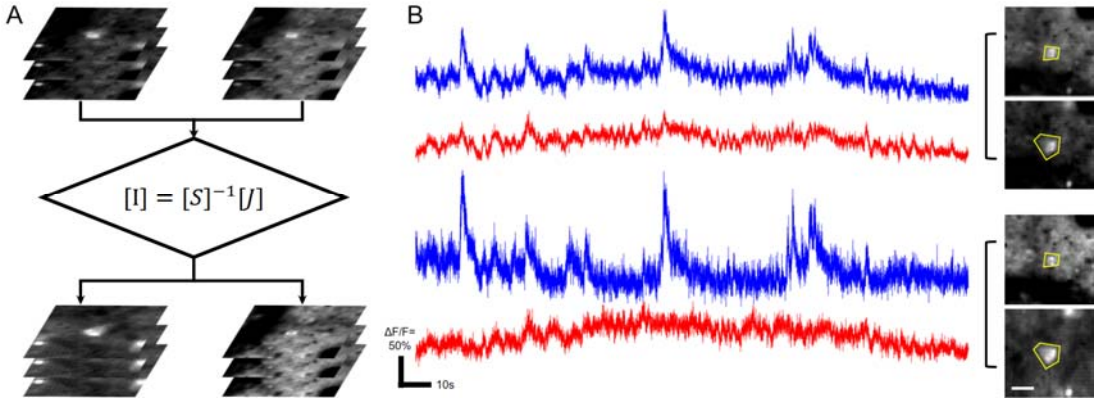

Fig. S5. Activity traces of lateral overlap neuron from different axial depth. A. Diagram of image linear demixing. **B**. Activities of two lateral overlap neuron (blue: L2/3, red: L5) from different axial depth before(up) and after(down) linear demixing. Scale bar: 10 μm.

Fig. S6.

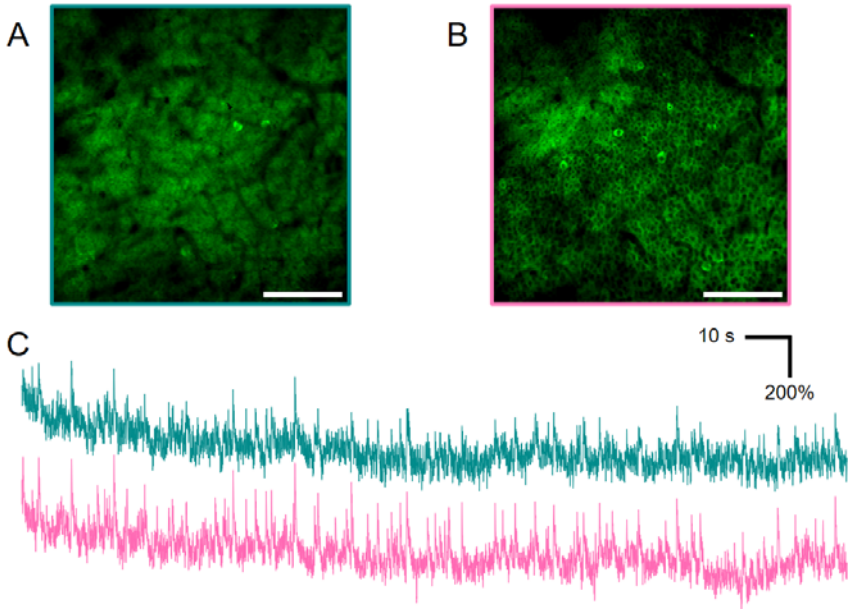

Fig. S6. Simultaneous dual plane imaging of GABA sensor signals. A. Averaged fields of view showing neurons expressing GABA sensor. 50 µm depth. Scale bar: 100 µm. **B.** Averaged fields of view showing neurons expressing GABA sensor. 100 µm depth. Scale bar: 100 µm. **C**. Z-score ΔF/F trace of GABA sensor activity from Plane 1(cyan) and Plane 2(pink). Imaging was performed on seizured mice (see Methods).

Fig. S7.

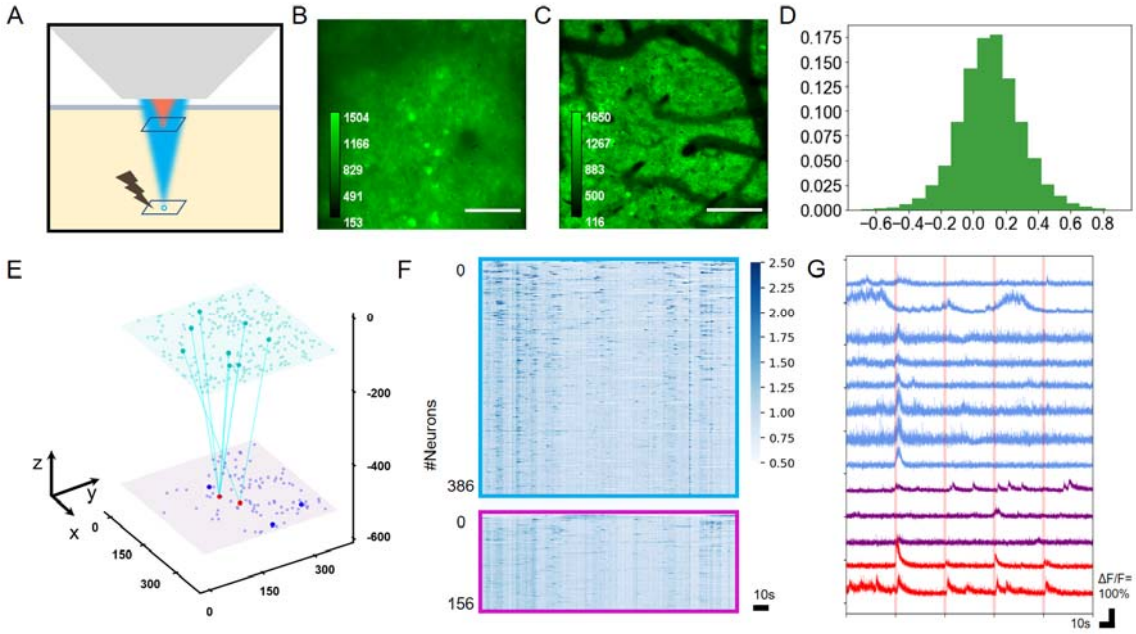

Fig. S7. Simultaneously dual plane recording and manipulating of mouse S1 neuronal activity. A. Diagram of dual plane imaging and two-photon photostimulation in mouse cortex. B**b**. Averaged fields of view showing neurons expressing GCaMP6s, 530 μm depth. Scale bar: 100 μm. **C**. Averaged fields of view showing neurons expressing GCaMP6s. 100 μm depth. Scale bar: 100 μm. **D**. Distribution of cross correlation coefficients of neural activities between two layers. **E**. 3D demonstration of all extracted neurons in micron. Lines between two planes indicate pairs of stimulated cells (red) and cells in response to activation (blue). Cells having response to activation in deeper plane are denoted (dark purple). **F**. Heat map of all neurons extracted from the recording in ΔF/F. Colors of frame denote layers. **G**. Traces of stimuli cells (red) in 530 μm depth and cells in response to activation in 100 μm and 530 μm depth (blue and purple).

Fig. S8.

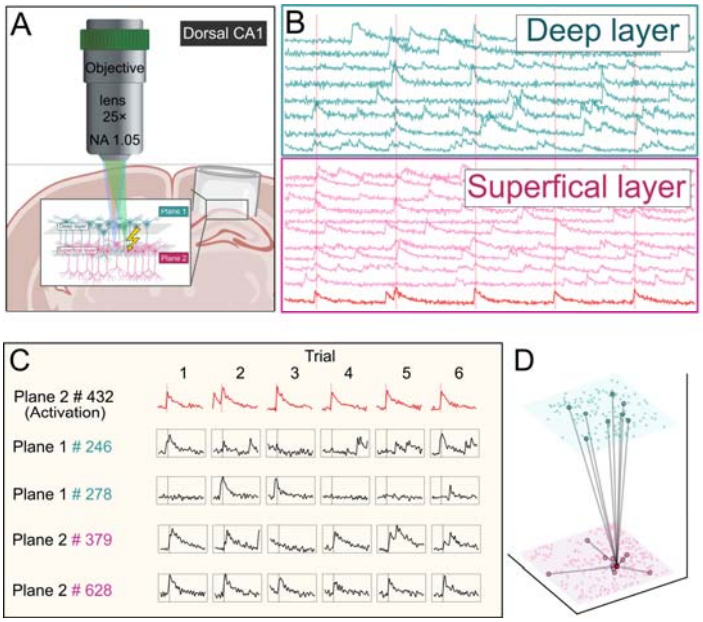

Fig. S8. CRAOP analysis on CA1 deep and superficial layers. A. Diagram of dual plane recording with optogenetic manipulation in mouse hippocampus CA1. **B.** Activities of selected neurons from the dual plane. (cyan: upper plane, pink: lower plane, red: target cell) **C.** Responses of the target neuron and other neurons to two-photon photostimulation. **D.** 3D demonstration of all recorded neurons from dual-plane recording with optogenetic manipulation. Lines connecting neurons indicate a high correlation between other neurons shown in (B) and the target neuron.

Fig. S9.

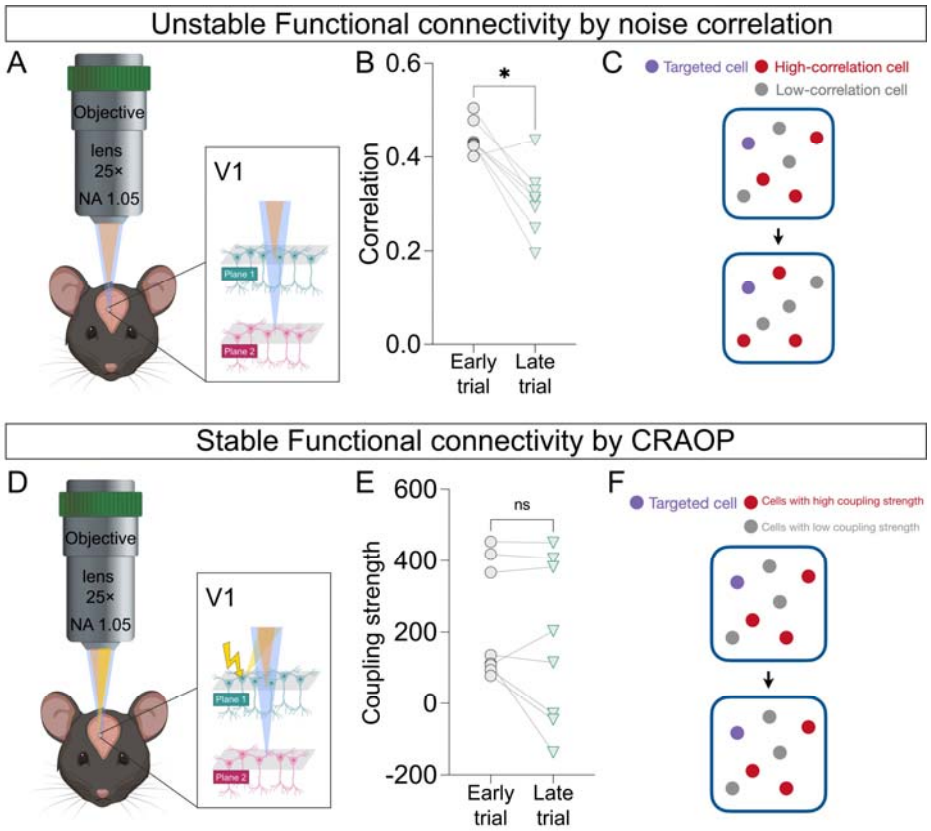

Fig. S9. More stable functional connectivity was dissected by CRAOP. (**A**) Diagram of dual plane recording in mouse cortex V1. Recordings were performed on two trials where no visual stimulus was presented. (**B**) In the early trial, neurons with top 10% correlation in activity with a selected cell were identified. The correlations significantly decreased in the late trial. (n=8 neurons) (**C**) Representative diagram showing noise correlations of neurons are not stable as time elapses. (**D**) Diagram of dual plane recording with optogenetic manipulation in mouse cortex V1. Recordings and optogenetics stimulations on the selected cell were performed on two trials where no visual stimulus was presented. (**E**) In the early trial, neurons with top 10% coupling strength with the targeted cell were identified. The coupling strengths remained high in the late trial. (n=8 neurons) (**F**) Representative diagram showing coupling strengths dissected by CRAOP are relatively stable as time elapses. n.s. Non-significant, *P < 0.05; Two-tailed Wilcoxon signed-rank test (B and E).

Fig. S10.

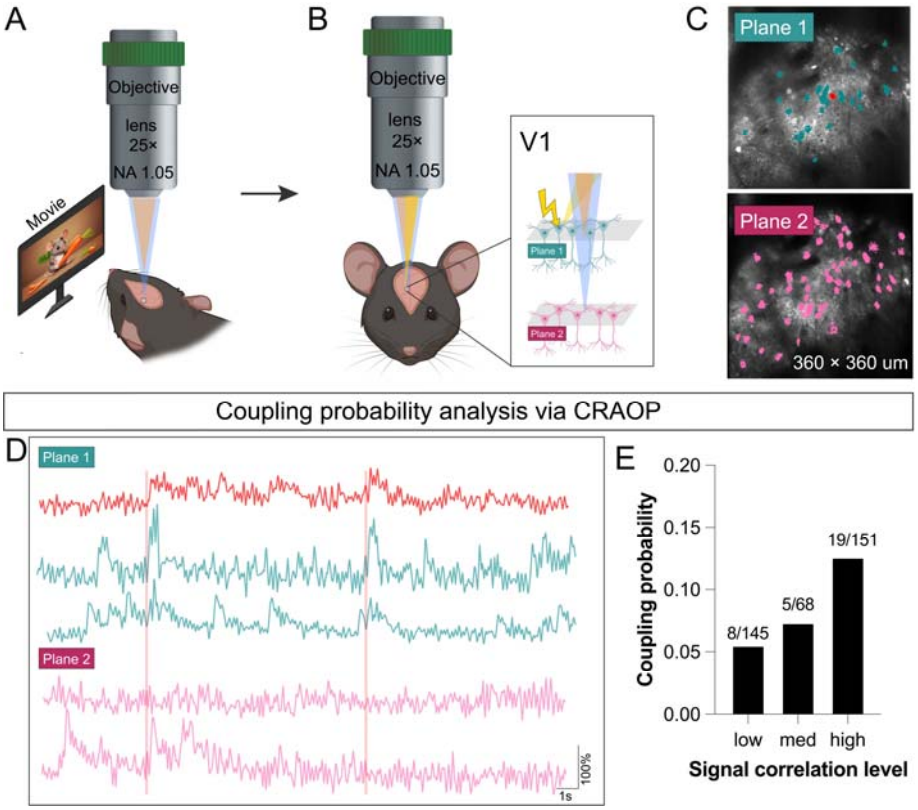

Fig. S10. CRAOP analysis of functional connectivity with natural movies as visual stimuli correlation in V1. (**A**) Diagram of dual plane recording in V1 with movies as visual stimuli. (**B**) Diagram of dual plane recording and targeted photostimulation in V1. (**C**) Example of spatial masks of recorded neurons in one trial (cyan: upper plane cells, pink: lower plane cells, red: cell to be photostimulated). (**D**) Example of activity traces of selected neurons cyan: upper plane cells, pink: lower plane cells, red: cell to be photostimulated). Vertical lines indicate optogenetic stimulation. (**E**) A significant increase in coupling probability with increasing signal correlation to visual stimuli (P=0.032, Cochran–Armitage test for trend).

Table S1.

Extended data Table 1. Summary of experimental conditions

Figures	Sample Mouse strain/ brain region	Fluorescent label/Opsin label	Offset lens (Focal length/ mm)	Objective	Frame rate (Hz)	Imaging power (Plane 1-Plane2/mW)	Activation Power/sti_duration x reps
2(a-e)	Ai162/ V1 cortex	GCaMP6s	75	CFI75 LWD 16X W	60	60-179	
2(f-j)	B6/CA1	GCaMP8m	250	XLPLN25XSVMP2	60	24-24	
2(k-n)	Ai162/ S1 cortex	GCaMP6s	250	XLPLN25XSVMP2	396.1	22-26	
2(o-s)	Ai162/ S1 cortex	GCaMP6s	75	CFI75 LWD 16X W	30/10	75-195	
3(a-d)	Thy1-GCaMP6s/CA3	GCaMP6s/ChRmine	250	XLPLN25XSVMP2	60	43-108	128 mW/100x1 ms
3(e-j)	B6/CA1	JEDI2p/C1V1	250	XLPLN25XSVMP2	396.1	88-107	128mW/100x 10 ms
3(i-n)	Ai162/ S1 cortex	GCaMP6s/ C1V1	75	CFI75 LWD 16X W	30/10	75-195	153mW/100x 10 ms
4(a-d)	B6/ V1 cortex	GCaMP8m/rsChRmine	250	XLPLN25XWMP2	60	56-104	
4(e-g)	B6/ V1 cortex	GCaMP8m/rsChRmine	250	XLPLN25XWMP2	60	56-104	170mW/100x 4 ms
5(a-g)	Ai162/ V1 cortex	GCaMP6s/ C1V1	250	XLPLN25XWMP2	60	42-63	
5(h-n)	Ai162/ V1 cortex	GCaMP6s/ C1V1	75	CFI75 LWD 16X W	30	28-137	153mW/100x 5 ms
S6	/CA1	GABA	250	CFI75 LWD	60	45-45	

		sensor		16X W			
S7	Ai162/ S1 cortex	GCaMP6s	75	CFI75 LWD 16X W	60	60-179	153mW/100x 10 ms
S8	B6/CA 1	GCaMP8m	250	XLPLN25XS VMP2	60	24-24	
S10	B6/ V1 cortex	GCaMP8m /rsChRmin e	250	XLPLN25XW MP2	60	56-104	170mW/100x 3 ms

Movie S1.

High frame rate (396.1Hz) dual plane imaging of GCaMP6s-labeled neurons in layer2/3 of the mouse sensory cortex. The pixel number of this video is 256 x 24.

Movie S2.

Dual plane recording with optogenetic manipulation in mouse hippocampus CA1. We conducted continuous imaging with 9 trials of stimulus. The pixel number of this video is 256 x 256.

Appendix:

For temporal multiplexing imaging of N planes, detected signal [J] can be described as following equations:

$$J_1(x,y) = S_{1,1}(x,y) \times I_1(x,y) + \cdots + S_{1,N}(x,y) \times I_N(x,y)$$

$$J_2(x,y) = S_{2,1}(x,y) \times I_1(x,y) + \cdots + S_{2,N}(x,y) \times I_N(x,y)$$

...

$$J_N(x,y) = S_{N,1}(x,y) \times I_1(x,y) + \ldots + S_{N,N}(x,y) \times I_N(x,y)$$

(1)

Here, $S_{i,j}$ is channel crosstalk from plane j to channel i , and following equation holds:

$$S_{1,1} + S_{2,1} + \cdots + S_{N,1} = 1$$

$$S_{1,2} + S_{2,2} + \cdots + S_{N,2} = 1$$

...

$$S_{1,N} + S_{2,N} + \ldots + S_{N,N} = 1 \qquad (2)$$

Thus, original signal [I] from different planes can be calculated as:

$$[I] = [S]^{-1}[J] \qquad (3)$$

For our dual plane imaging configuration, detected signal [J] of each channel can be described as following equations:

$$J_1(x,y) = S_{1,1}(x,y) \times I_1(x,y) + S_{1,2}(x,y) \times I_2(x,y)$$

$$J_2(x,y) = S_{2,1}(x,y) \times I_1(x,y) + S_{2,2}(x,y) \times I_2(x,y)$$

(4)

Elements of crosstalk [S] can be determined based on individually imaging results of lower plane and upper plane. It can also be determined by looking for a coefficient that minimizes the correlation of the demodulated images. The matrix [S] changes with different indicators and varying bandwidth of transimpedance amplifier. In our experiment, lower cut-off frequency of transimpedance amplifier leads to higher SNR of imaging results. However, high signal aliasing will also increase the amplitude of additive noise. Considering the actual situation with noise N_i on each channel:

$$\begin{bmatrix} I_1 + N_1(\sigma_{I_1}) \\ I_2 + N_1(\sigma_{I_2}) \end{bmatrix} = \frac{1}{S_{1,1}+S_{2,2}-1} \begin{bmatrix} S_{2,2} & S_{1,1}-1 \\ S_{2,2}-1 & S_{1,1} \end{bmatrix} \begin{bmatrix} J_1 + N(\sigma_{J_1}) \\ J_2 + N(\sigma_{J_2}) \end{bmatrix}$$

(5)

When $S_{1,1}$ and $S_{2,2}$ are nearly 1, it is close to the ideal situation without signal aliasing. The amplification effect of noise is negligible. However, when $S_{1,1}$ and $S_{2,2}$ are approaching 0.5 (totally aliasing), noise of recovered signal may be amplified gradually. Taking plane 1 as an example:

$$\sigma_{I_1} = \frac{1}{S_{1,1}+S_{2,2}-1}\sqrt{(S_{2,2}\sigma_{J_1})^2 + (S_{1,1}-1)^2{\sigma_{J_2}}^2} \quad (6)$$

Assuming $S_{1,1} = S_{2,2} = 0.7$ and $\sigma_{J1} = \sigma_{J2} = \sigma$, we get $\sigma_{I1} = 1.90\ \sigma$, which means that noise is amplified compared to aliased raw image. Adopting a data acquisition board with a high sampling rate (up to GHz) or reducing the repetition rate of the femto-second laser may reduce channel crosstalk and improve the performance of temporal multiplex imaging.

To demonstrate that our system can realize dual-plane neural activity recording without the need for image sparsity or prior knowledge. We select two neurons that have lateral overlap but from different axial plane (100 μm and 530 μm). The raw data is first redistributed by linear demixing (**fig. S5A**). Averaged images of two neurons and the corresponding calcium signal are shown in **fig. S5B**. It is shown that neuron activities of two lateral overlap neurons can be extracted distinctly. The correlation coefficient of traces from raw data is 0.8177, which indicates high aliasing before linear demixing. However, the correlation coefficient of traces is reduced to -0.0904, which shows that the calcium signal of two neurons can be reliably recorded.